

INFRARED EXCESS AND MOLECULAR CLOUDS: A COMPARISON OF NEW SURVEYS OF FAR-INFRARED AND H I 21 CENTIMETER EMISSION AT HIGH GALACTIC LATITUDES

WILLIAM T. REACH

Institut d'Astrophysique Spatiale, Université Paris Sud, F-91405 Orsay cedex, France; Infrared Processing and Analysis Center, California Institute of Technology, MS 100-22, Pasadena, CA 91125

WILLIAM F. WALL

Instituto Nacional de Astrofísica, Óptica, y Electrónica, A. Postal 51 y 216, Puebla, Puebla, Mexico

AND

NILS ODEGARD

Raytheon STX Corporation, 4400 Forbes Boulevard, Lanham, MD 20706

Received 1998 February 16; accepted 1998 June 15

ABSTRACT

We have created a map of the large-scale infrared surface brightness in excess of that associated with the atomic interstellar medium, using region-by-region correlations between the far-infrared and 21 cm line surface brightness. Our study updates and extends a previous attempt with the *Infrared Astronomical Satellite* and Berkeley/Parkes H I surveys; in this study we used far-infrared (60–240 μm) data from the *Cosmic Background Explorer* Diffuse Infrared Background Experiment and 21 cm data from the combined Leiden-Dwingeloo and Parkes 21 cm line surveys. Using the maps of excess infrared emission at 100, 140, and 240 μm , we created an atlas and identified the coherent structures. These infrared excess clouds can be caused both by dust that is warmer than average or by dust associated with gas other than the atomic interstellar medium. We find very few warm clouds—which are relatively bright at 60 μm —such as the H II region around the high-latitude B-type star α Vir and a new cloud of unknown origin that we name DIR 015+54. Using the ratio of 100 to 240 μm brightness, we find that infrared excess clouds are *cold*. The dust temperature in atomic gas is 19 ± 2 K, while the dust temperature in known high-latitude molecular clouds (all of which have infrared excess) is 15.5 ± 1 K. The dust temperature in those infrared excess clouds that are not known to be associated with molecular clouds (generally because they have never been observed) is 17 ± 2 K, suggesting they are similar to high-latitude molecular clouds. Infrared excess clouds are peaks of column density rather than dust temperature, and their excess infrared emission is likely due to dust associated with molecular gas. For a large region in Ursa Major-Ursa Minor-Camelopardalis, where the CO(1 \rightarrow 0) line has been surveyed, we correlated the infrared excess CO line integral, allowing us to measure $X = N(\text{H}_2)/W(\text{CO}) = (1.3 \pm 0.2) \times 10^{20} \text{ cm}^2 (\text{K km s}^{-1})^{-1}$ for high-latitude molecular clouds. Our measurement of X takes into account the low dust temperature in molecular gas; this correction amounts to a factor of 3.8 increase in the X -value that would naively be determined using only 100 μm , CO, and H I data. Our value of X is consistent with a recent γ -ray determination for the same region, while it is a factor of about 2 lower than the value determined for the inner galactic plane. The surface mass density of infrared excess clouds is $0.3 M_{\odot} \text{ pc}^{-2}$. The atlas of infrared excess clouds may be useful as a guide to regions of relatively high interstellar column density, which might extinct light from extragalactic objects at optical to ultraviolet wavelengths and confuse structures in the cosmic background at infrared to microwave wavelengths.

Subject headings: diffuse radiation — infrared: ISM: continuum — ISM: clouds — ISM: molecules — radio lines: ISM

1. INTRODUCTION

It has been known for some time that interstellar molecular gas exists away from the galactic midplane, based on the presence of absorption lines of H₂ and other molecules in the spectra of high-latitude stars (Savage et al. 1977) and the presence of millimeter-wave emission of CO from regions of high optical extinction (Blitz, Magnani, & Mundy 1984). However, the pervasiveness of the molecular component of the local interstellar medium has not been convincingly assessed, because of the difficulties of observing molecular gas over large areas. Absorption-line observations are restricted either to trace elements or to lines of sight toward the few hot, bright stars at high latitude, because the electronic ground-state transitions of both atomic and molecular hydrogen are in the ultraviolet. Millimeter-wave observations of CO are restricted to relatively small areas

because all-sky observations are at present prohibitively expensive. An early survey of randomly selected lines of sight found a surface filling fraction of 0.5% for CO(1 \rightarrow 0) emission (Magnani, Lada, & Blitz 1986). A large, but necessarily incompletely sampled, survey was recently performed with a very low detection rate of 0.3%, suggesting that the northern Galactic hemisphere is largely “devoid” of molecular gas (Hartmann, Magnani, & Thaddeus 1997). On the other hand, there remains the question of whether a survey in a particular observable quantity, such as the brightness of collisionally excited rotational line emission of a particular molecule, is really tracing all of the molecular gas. The H₂ and CO might have somewhat different spatial distributions because of their different photodissociation cross sections and chemistry, and the rotational energy levels of CO may not be excited in low-density [$n(\text{H}_2) < 10^3 \text{ cm}^{-3}$]

environments.

With the advent of the infrared all-sky survey by the *Infrared Astronomical Satellite (IRAS)*, a new light was cast on the study of the interstellar medium (Neugebauer et al. 1984; Low et al. 1984). The 100 μm surface brightness was found to be well correlated with the H I column density on both small and large scales (Boulanger & Pérault 1988), demonstrating its value as a tracer of interstellar gas. If the infrared emission arises from both the atomic and molecular phases of the interstellar medium, then regions with excess infrared emission relative to the H I column density are likely locations of molecular gas. This effect has been demonstrated in Ursa Major (de Vries et al. 1987) and for isolated cirrus clouds (Heiles, Reach, & Koo 1988; Reach, Koo, & Heiles 1994); in both cases the infrared excess was found to be associated with CO emission. Because the infrared surface brightness and H I column density are known over the entire sky, it is possible to use the difference between the infrared map and an appropriately scaled map of H I column density to produce an all-sky survey of molecular gas. This idea has been exploited by Désert, Bazell, & Boulanger (1988), who used the *IRAS* 100 μm data and the Berkeley H I survey (Heiles & Habing 1974) to create a catalog of infrared excess clouds.

In the present paper, we study the distribution and nature of infrared excess clouds using relatively recent data from the *Cosmic Background Explorer*¹ (*COBE*) mission (Boggess et al. 1992) and the Leiden-Dwingeloo H I survey (Hartmann & Burton 1997). These new surveys provide higher sensitivity and higher reliability than the previous infrared and H I observations for large-scale emission. More importantly, the *COBE* observations at 100, 140, and 240 μm wavelengths are a reliable measure of the emission from the large, thermal equilibrium grains that dominate the dust mass (Désert, Boulanger, & Puget 1990). From a detailed study of the infrared emission in the Orion region, it was shown that the 100, 140, and 240 μm emission sample essentially the same dust (Wall et al. 1996). Our first results (Reach et al. 1994), based on comparing the *COBE* 240 μm optical depth with the Berkeley H I surveys, encouraged us to pursue a more thorough comparison of the H I and infrared data.

The large-scale distribution of molecular gas is important for a number of practical applications.

Extinction of extragalactic objects.—Extragalactic observations at visible and shorter wavelengths are affected by extinction even at high galactic latitude. In order to estimate the extinction, which affects both the brightness and color of extragalactic objects, it has been necessary to rely on 21 cm line surveys (cf. Burstein & Heiles 1978). If an extragalactic object lies behind a high-latitude molecular cloud, its extinction will be significantly underestimated using the 21 cm line surveys. The results derived here will help observers to identify regions where anomalously high extinction from molecular clouds can be expected. A recent effort by another group (Schlegel, Finkbeiner, & Davis 1997) systematically addresses this issue, using the *COBE* and *IRAS* data to create a map of the extinction. Large-

scale variations in the temperature and gas-to-dust ratio were calibrated by Schlegel et al. in a manner very similar to ours. By calculating the column density using large-scale average dust temperature, it is likely that the Schlegel et al. dust maps will underestimate the extinction toward relatively cold clouds such as the molecular clouds we have identified. We therefore recommend that the Schlegel et al. maps be used to estimate the extinction and that our molecular cloud atlas be used as a supplement, warning of cold, high-extinction clouds. Lines of sight behind these clouds should certainly be avoided unless 1–3 mag (A_V) of extinction can be tolerated.

Shadowing of distant X-rays.—Interstellar clouds produce distinct shadows on the soft X-ray emission from the Galactic halo and the extragalactic emission (McCammon & Sanders 1990). These shadows have been compared with 21 cm line maps and with *IRAS* 100 μm surface brightness maps (Snowden, McCammon, & Verter 1993; Wang & Yu 1995). In both cases, the interstellar column density is underestimated in the presence of molecular clouds, because molecular gas can absorb X-rays and molecular clouds are relatively faint at 100 μm (and nearly invisible at 60 μm ; Laureijs et al. 1996), compared with atomic gas. We provide both a map of infrared excess clouds and a calibration of their column density in the present paper.

Diffuse γ -ray emission and the $N(\text{H}_2)/W(\text{CO})$ factor.—A significant source of the γ -ray surface brightness of the sky is due to interaction of cosmic rays with interstellar gas. The expected near-linear proportionality of γ -rays with total column density allows a calibration of the molecular column density, when correlated with H I and CO maps (Strong et al. 1988; Digel et al. 1996). In the presence of H_2 clouds with relatively little CO emission, this calibration can be significantly biased. Here we calibrate the molecular column density using the infrared excess and compare the results with γ -ray studies. The ratio of the H_2 column density to the CO line integral is important for assessing the vertical mass distribution of molecular gas in the disk of our Galaxy.

Relation to external galaxies.—Molecular regions in low-metallicity galaxies such as the Large and Small Magellanic Clouds are very different from giant molecular clouds in our Galaxy, because of the lack of dust and stronger radiation field. The extremely high ratio of C^+/CO line brightness (Mochizuki et al. 1994) suggests that Magellanic molecular regions are more translucent. Local high-latitude molecular clouds, such as those studied in this paper, share some empirical similarities with low-metallicity galaxies and should provide insight into the nature of the latter.

2. THE CORRELATION OF FAR-INFRARED EMISSION WITH H I

2.1. Observations

The far-infrared data used in this work originate from the Diffuse Infrared Background Experiment (DIRBE) (Hauser et al. 1997). The DIRBE produced a redundantly sampled all-sky survey in 10 wave bands from the near to far-infrared; here we concentrate on the 100, 140, and 240 μm wave bands, which are dominated by the emission from interstellar dust. In particular, these wave bands are dominated by the emission from the larger grains, in thermal equilibrium with the interstellar radiation field, that domi-

¹ The National Aeronautics and Space Administration Goddard Space Flight Center (NASA GSFC) is responsible for the design, development, and operation of the *Cosmic Background Explorer (COBE)*. Scientific guidance is provided by the *COBE* Science Working Group. GSFC is also responsible for the development of the analysis software and for the production of the mission data sets.

nate the mass of dust in the interstellar medium. Nonetheless, a significant source of large-scale emission, even in the far-infrared, is from the zodiacal light. For this work, we use data from which a model for the zodiacal light has been subtracted (Reach et al. 1996; Kelsall et al. 1998). To minimize detector noise, which is significant for the 140 and 240 μm wave bands, we use the average of the zodiacal light-subtracted weekly maps over the cold mission (44 weeks). The instantaneous beam size of DIRBE is $42'$. In order to avoid confusion between the interstellar clouds that we hope to study and bright infrared point sources, we use data from which all pixels containing bright and apparently unresolved structure, as well as circular regions around the Magellanic Clouds, have been masked (Arendt et al. 1998). Furthermore, we will not consider here the portion of the sky close to the galactic plane ($|b| < 20^\circ$), where clouds from a wide range of distances overlap on the sky. The DIRBE data are gridded into a sky-cube projection, which we degraded to a pixel size of $39'$ so that each pixel is nearly independent. We assume that the point-to-point uncertainty in the infrared surface brightness at (100, 140, 240 μm) is a quadrature combination of (0.15, 1.3, 0.75 MJy sr^{-1}) and 2% of the surface brightness, to account for detector noise, pixelization uncertainties, source confusion, and gain drifts. These uncertainty estimates were determined from inspection of the data. At 140 and 240 μm the point-to-point uncertainty is comparable to the expected instrument noise (cf. Hauser et al. 1998), but at 100 μm it is significantly larger, so we must have included some of the detected small-scale sky structure of the interstellar medium. The uncertainties are important in the present work mostly for weighting the data, but they do scale the χ^2 statistics.

The H I 21 cm line data used in this work originate from the Leiden-Dwingeloo survey of the northern sky (Hartmann & Burton 1997) and the Parkes survey of the southern sky (Cleary et al. 1979). The Dwingeloo 25 m telescope has a main beam size of $36'$, which is well matched to the DIRBE beam size. An important aspect of the Leiden-Dwingeloo survey is the removal of stray radiation, which is up to half of the observed signal at high galactic latitudes. The near and far sidelobes of the telescope response were mapped using bright point sources, then the sidelobe emission was estimated by convolving the skymap with the beam (Hartmann et al. 1996). For this work we use the integrated 21 cm line brightness, converted into H I column density assuming the emission is optically thin. This latter assumption is unlikely to be violated at high galactic latitude unless the H I gas is colder than 20 K. Gas this cold must be well shielded from the interstellar radiation field, or else photoelectric heating will raise its temperature to at least 50 K at typical interstellar pressure (Kulkarni & Heiles 1988). In such cold, shielded regions, the H I is rapidly converted into H_2 , so that the H I column density becomes a negligible fraction of the total. We integrated the H I line over the range of -100 to $+100$ km s^{-1} , which includes the bulk of local interstellar gas but excludes high-velocity clouds. The high-velocity clouds have been shown to be deficient in interstellar dust (Wakker & Boulanger 1986); therefore they can be ignored in the present study. For declinations south of -30° , we used the 21 cm survey performed with the Parkes 64 m telescope (Cleary et al. 1979). The Parkes survey provides critical information on the southern sky, but it does suffer from undersampling (every

beamwidth in right ascension but every other beamwidth in declination) and incompleteness (some survey scans missing). Furthermore, the Parkes survey has not been corrected for stray radiation. We checked the calibration of the Parkes and Leiden-Dwingeloo surveys by comparing their column densities where the surveys overlap; the calibrations were in good agreement. We assume the point-to-point uncertainty in the H I column density is a quadrature sum of 1×10^{19} cm^{-2} and 2% of the column density, to account both for uncertainties in the stray radiation and the gain. The uncertainties were not rigorously determined; they are based on the estimated gain and stray radiation accuracy (Hartmann & Burton 1997).

2.2. Region-by-Region Correlations

In order to identify molecular clouds in the infrared maps, we must first remove the infrared emission from dust associated with the atomic interstellar medium. We presume the column density of the atomic interstellar medium is linearly traced by the integrated 21 cm line brightness. The infrared emission, however, is not a linear tracer of the interstellar dust because it is sensitive to the dust temperature. We considered two methods to calibrate the dust temperature variations: (1) calculate the column density at each pixel using the 100, 140, and 240 μm brightness ratios assuming a single dust temperature along the line of sight, and (2) calculate the ratio of infrared to H I surface brightness from region to region on the sky. The first method is simpler and, in principle, it could detect temperature changes on angular scales as fine as 1° . But in practice the 140 and 240 μm maps are very noisy and the 100 μm map suffers from large angular scale zodiacal light residuals (and all wavelengths contain some cosmic infrared background radiation). Furthermore, we show below that the dust associated with molecular gas is significantly colder than that associated with atomic gas, so that a single dust temperature does not apply to the lines of sight we are most interested in. Therefore, we used the second method, by dividing the sky into “cells,” with 10° radius, on a regular grid every 10° . Within each cell, we measured the slope and intercept of the pixel-to-pixel infrared surface brightness as a function of H I column density. To illustrate the procedure, Figure 1 shows an example. In the upper panel, we show the 240 μm surface brightness versus H I column density for the entire dynamic range of both quantities, within the region 15° in radius centered on galactic coordinates $(l, b) = (140^\circ, 35^\circ)$.

At low H I column densities there is a linear rise of infrared surface brightness with H I column density, while at higher column densities there is a wide dispersion. This dispersion is due to infrared emission associated with gas other than H I. At low column density, interstellar H remains atomic, but where the column density is large, the H becomes molecular. For a uniform-density cloud, the H_2 column density is predicted to exceed the H I column density when

$$N(\text{H I}) > 2.5 \times 10^{20} \left(\frac{n}{100 \text{ cm}^{-3}} \right)^{-2} \left(\frac{T}{80 \text{ K}} \right)^{-1} \text{ cm}^{-2} \quad (1)$$

(Reach et al. 1994). In low-density regions, H_2 cannot form, while in denser clouds such as account for the 21 cm absorption features in front of radio sources (see review by Kulkarni & Heiles 1988), the gas readily forms molecules at

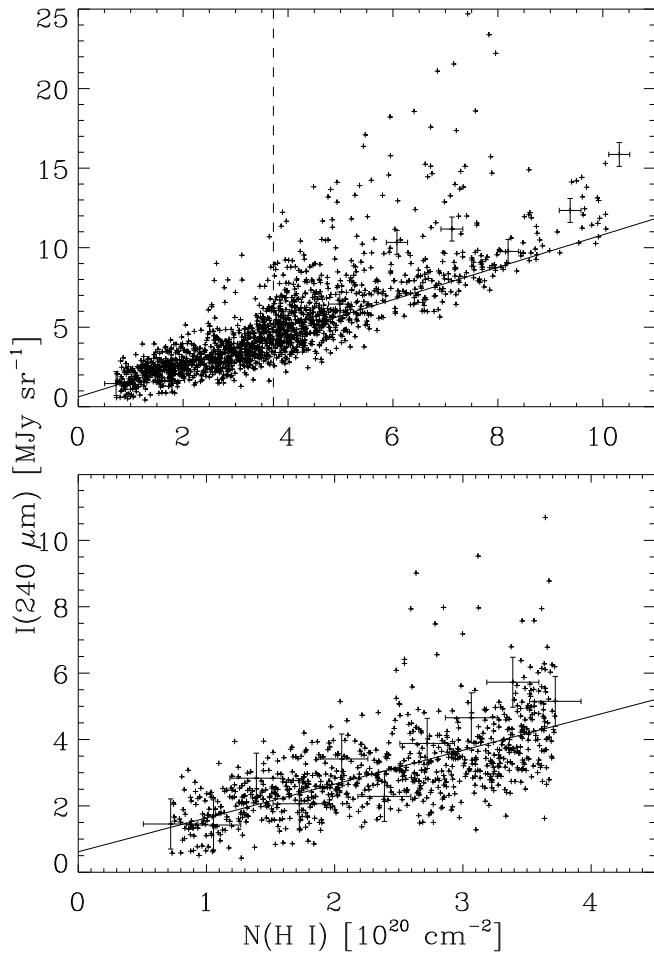


FIG. 1.—Infrared surface brightness at $240\ \mu\text{m}$ observed by DIRBE plotted vs. the atomic gas column density from the Leiden-Dwingeloo 21 cm line survey for the Ursa Major-Ursa Minor-Camelopardalis region. In the top panel, nearly the full dynamic range of H I and infrared brightness is shown; 56 points, out of 2393 total, with $N(\text{H I}) > 1.6 \times 10^{21}\ \text{cm}^{-2}$ were excluded. Error bars are shown for a few points for illustration. The vertical dashed line indicates the threshold column density below which a linear fit was performed. The bottom panel shows the same data, but with restricted dynamic range covering only the points used in the fit, $N(\text{H I}) < 3.75 \times 10^{20}\ \text{cm}^{-2}$. The linear fit to the low column density points is shown in both panels as a diagonal solid line. In this paper we concentrate on the positive residuals from the linear fits, which we attribute to dust associated with ionized and molecular gas.

column densities $> 3 \times 10^{20}\ \text{cm}^{-2}$. Figure 1 shows this effect: the points at higher H I column densities deviate systematically upward from the straight line fitted to the lower column density points. This upward deviation, presumably due to infrared emission from dust associated with molecular gas, is what we will call the “infrared excess.” We presume that on large scales, the warm and cold phases of

the interstellar atomic gas exist in pressure equilibrium and the cold clouds have a relatively small filling factor, so that all lines of sight cross warm regions and some (or all) cross cold regions. In order to exclude cold clouds with column densities sufficient to form H_2 from our infrared-H I correlations—which are intended to measure the properties of the atomic medium only—we exclude all points with a column density more than $3 \times 10^{20}\ \text{cm}^{-2}$ above the minimum column density for the “cell.” The minimum column density is presumed to represent the warm H I, and by allowing a different threshold in each cell we allow for the longer path length through the warm gas Galaxy at low latitudes. The threshold column density for the Ursa Major-Ursa Minor-Camelopardalis region is shown as a vertical dashed line in Figure 1.

For the low column density pixels within a given sky “cell,” we perform a linear fit of infrared surface brightness versus H I column density, taking into account the uncertainties in both quantities. For the sample cell, the points used in the fit and their uncertainties are shown in the lower panel of Figure 1. Even at low column densities, there are some outlying positive points, but in no case do the fits appear to be biased by outliers. The resulting slope and intercept for two sample cells, widely separated on the sky, are shown in Table 1. In both cases the fits are “good” in the sense that the reduced χ^2_ν is essentially unity (to within our understanding of the measurement uncertainties). At $240\ \mu\text{m}$, the infrared-H I slopes of the two cells are similar, but at $100\ \mu\text{m}$ the slopes are significantly different. Using the ratio of slopes at 100 and $240\ \mu\text{m}$, (and assuming the interstellar dust emissivity varies as ν^2 ; Draine & Lee 1984), we find that the temperature of the dust associated with H I is $17.2 \pm 0.2\ \text{K}$ in the cell centered on $(140^\circ, 35^\circ)$, and $19.0 \pm 0.3\ \text{K}$ in the cell centered on $(40^\circ, 35^\circ)$. Even though a $2\ \text{K}$ temperature difference between the two cells may seem unimportant, a change in temperature from 17 to $19\ \text{K}$ increases the emission at $100\ \mu\text{m}$ by a factor of 2.4 and the $240\ \mu\text{m}$ emissivity by a factor of 1.7 , so that the ratio of $100/240\ \mu\text{m}$ emission increases by 60% . The ratios of dust optical depth at $100\ \mu\text{m}$ (assuming ν^2 emissivity) to gas column density in the two cells are 6.4 and 4.6 , respectively, in units of $10^{-25}\ \text{cm}^2$. The absolute calibration uncertainty is $\pm 15\%$ in these dust-to-gas ratios, but the uncertainty in cell-to-cell variations is much less. Therefore, the (30%) difference between the dust-to-gas ratios in atomic gas in these cells is statistically significant.

We have calibrated the differences in the dust temperature and dust-to-gas ratio in atomic gas from region to region by performing independent fits of the infrared surface brightness as a function of H I column density at each wavelength and in each sky cell. These fit parameters were well constrained for most of the sky, but there were some regions where the infrared emission was relatively

TABLE 1
INFRARED TO H I CORRELATIONS FOR TWO REGIONS (OR “CELLS”)

WAVELENGTH (μm)	$(l, b) = (140^\circ, 35^\circ)$			$(l, b) = (40^\circ, 35^\circ)$		
	Slope ($\text{MJy sr}^{-1}/10^{20}\ \text{cm}^{-2}$)	Offset (MJy sr^{-1})	χ^2_ν	Slope ($\text{MJy sr}^{-1}/10^{20}\ \text{cm}^{-2}$)	Offset (MJy sr^{-1})	χ^2_ν
100	0.56 ± 0.01	0.63 ± 0.02	1.25	0.89 ± 0.01	0.33 ± 0.04	1.77
140	1.12 ± 0.06	1.01 ± 0.14	1.06	1.45 ± 0.06	0.44 ± 0.21	0.91
240	1.02 ± 0.03	0.62 ± 0.08	1.26	1.07 ± 0.04	0.42 ± 0.12	0.91

poorly correlated with the H I, even at low column densities. If a molecular cloud complex or dust hot spot is comparable to or larger than our cell size (10°), then it is not possible to calibrate the infrared–H I slope. These regions are generally near the galactic plane, and for the most part they can be identified with well-known star-forming complexes. For each of these complexes, a detailed study using higher resolution maps is needed to sort out the variations in gas phase and dust heating due to embedded stars (e.g., Boulanger et al. 1998 for the Chameleon complex).

All-sky maps of the infrared–H I slope and offset at $100\ \mu\text{m}$ are shown in Figure 2. In cells where the fits were found to be poor, we interpolated using adjacent cells. In cells where the fit is good, we interpolated to a finer, $37'$ grid in order to avoid discontinuities at cell boundaries. Two regions that stand out in the infrared–H I slope are at $(300^\circ, +50^\circ)$ and $(90^\circ, -40^\circ)$. The former is due to the effect of the nearby, early-type star Spica, whose situation at high latitudes allows it to heat dust over a very large apparent area

(Reynolds 1985), while the latter is due to the MBM 53/54/55 complex of molecular clouds (Magnani et al. 1985). Our cell size was chosen so that regions like these would not completely disappear once the infrared emission associated with H I is subtracted. In addition to these relatively compact regions, there are real variations in the $100\ \mu\text{m}$ –H I slope due to temperature variations from place to place of the interstellar dust associated with atomic gas. These variations appear in Figure 2 as large-scale structures. One noticeable problem is at southern declinations, where the H I data from the Parkes survey was used. The infrared emission per H atom is lower there than average, which could be in part because of stray radiation effects in the Parkes survey.

2.3. Implications for the Far-Infrared Background

For each of the far-infrared wavelengths we have considered here, we find that a positive residual sky brightness remains after subtracting the infrared emission correlated

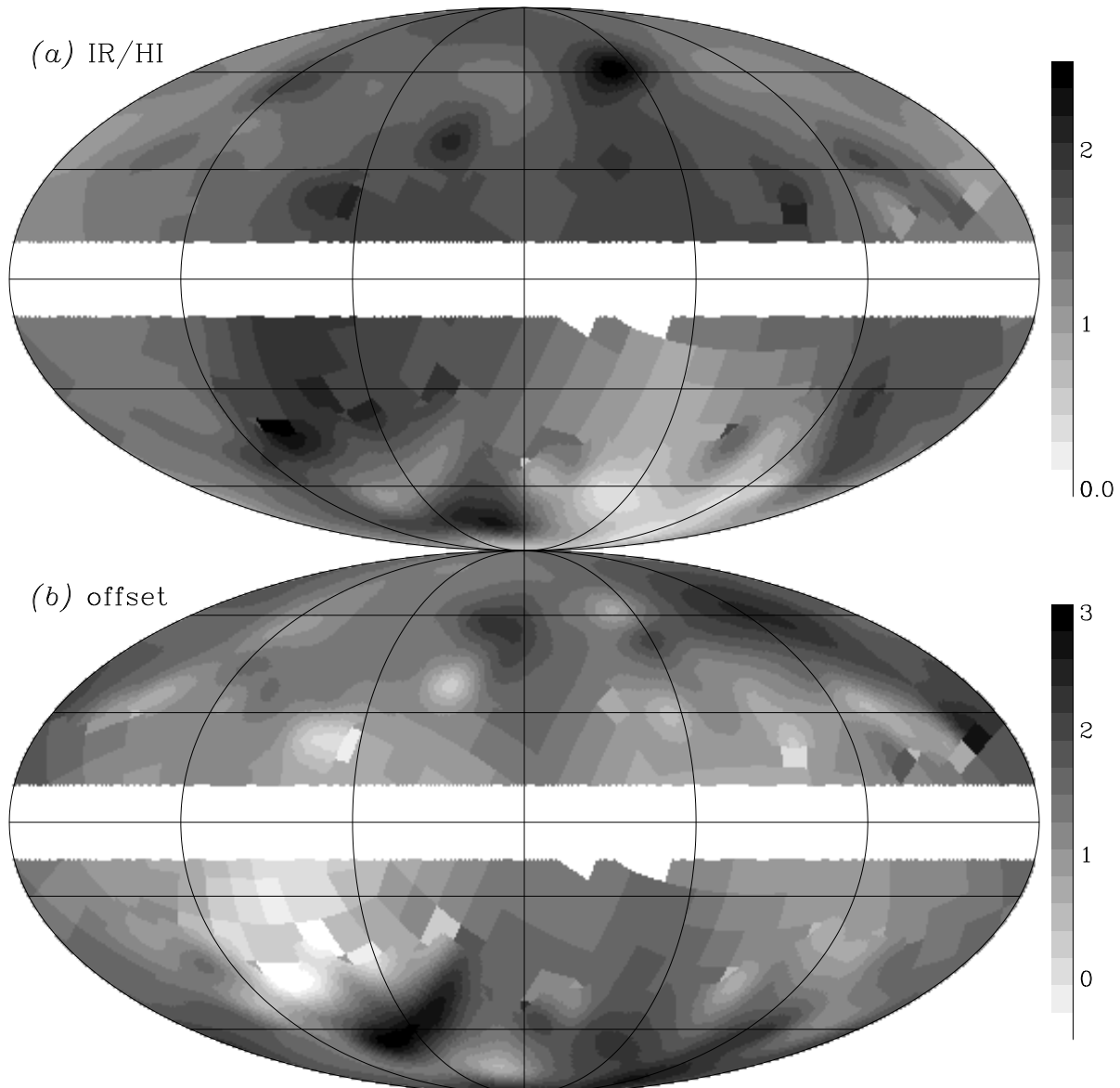


FIG. 2.—All-sky maps of the (a) slope and (b) offset of the correlation between $100\ \mu\text{m}$ surface brightness and H I column density. The maps are shown in a galactic coordinate Mollweide projection with the galactic center at the center. Meridians are drawn every 60° , and parallels are drawn every 30° . The gray-scale ranges are labeled to the right of the images; for panel a in $\text{MJy sr}^{-1}/(10^{20}\ \text{cm}^{-2})$ and for panel b in MJy sr^{-1} .

with the H I column densities. Histograms of all the zero intercepts of the infrared–H I correlation for our grid of sky cells are shown in Figure 4; it is clear that the zero intercept is consistently positive. This same result has also been found from the correlations of infrared brightness with H I column density in the Lockman Hole and around the north ecliptic pole (Arendt et al. 1998) and for the entire low column density portion of the northern sky (Boulanger et al. 1996). At least part of the residual emission is related to the solar system, because one can see the distinctive pattern of the ecliptic plane in Figure 2. However, the amplitude of the residual zodiacal light, based on its ecliptic latitude dependence, is small. Furthermore, the spectrum is inconsistent with the zodiacal light, being relatively bright at $240\ \mu\text{m}$, which argues against a solar system origin (Dwek et al. 1998). The far-infrared emission remaining after the subtraction of the emission from interstellar dust could be the extragalactic background due to unresolved galaxies, with obvious cosmological significance; alternatively, it could be due to a component of our galaxy with infrared emission but little atomic gas. We will address the cosmological issue only briefly here, as it is the primary focus of other recent papers (Puget et al. 1996; Hauser et al. 1998). In the present work, we have allowed for the possibility that the infrared emission per unit H I column density varies from place to place. In the presence of uncertainties in both variables, the slope and zero intercept of a correlation tend to be correlated. Because the H I column density is always positive, the slope and intercept are negatively correlated; furthermore, the intercept is biased toward positive values where the correlation is weak. Comparing the slope and offset of all of the sky cells with a significant fit, we find a near-perfect anticorrelation. This could potentially lead to a false detection of the cosmological background, especially if, at low column densities, the interstellar dust is associated with an interstellar medium other than atomic gas.

The infrared emission per unit H I column density has a well-defined mean value, with few regions of abnormally high or low values. Table 2 lists the mean and rms dispersion of the infrared emission per unit H I column density and the zero intercept of the infrared–H I correlation at 100, 140, and $240\ \mu\text{m}$. It is clear that the range of slopes and intercepts obtained over the high-latitude sky is significantly larger than the uncertainty of an individual value, so that the range of slopes is not due to random measurement or fitting uncertainties. The wavelength dependence of the slopes in the two sample regions (Table 1) indicates that this is mostly a dust temperature effect. This is a gradual, large-scale effect that is not confined to the few outstanding cells. The cells with an infrared–H I slope more than 1.5 times the rms away from the mean are shaded in Figure 3 and Figure 4. It is evident that the outlying regions in terms of infrared–

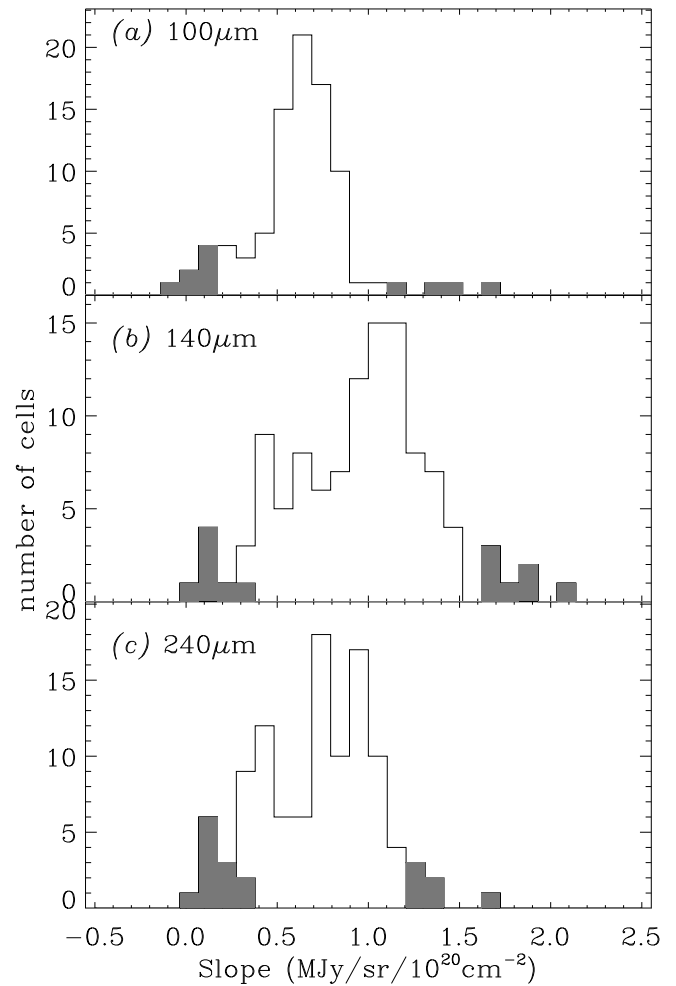


FIG. 3.—Histograms of the slopes of the infrared–H I correlations for sky patches with 10° radius. Each panel shows the results from a different DIRBE wave band: (a) $100\ \mu\text{m}$, (b) $140\ \mu\text{m}$, (c) $240\ \mu\text{m}$. The “outlying” values of the slope, defined as being more than 1.5 times the rms away from the mean, are shaded.

H I slope are also outlying in terms of the zero intercept (as expected because of the anticorrelation of slope and intercept mentioned above). Over the entire sky, there is a significant, positive sky brightness that cannot be explained by interstellar dust associated with H I.

If the range of slopes shown in Figure 3 is a *real* effect due to the interstellar medium, then the range of offsets in Figure 4 is also due to the Galaxy. The inferred brightness of an isotropic extragalactic background must then be lower than the *lowest* offset value. In principle, variations in the infrared–H I correlation on scales smaller than those chosen for the present work could lead to an even wider

TABLE 2
STATISTICS OF SLOPES AND INTERCEPTS^a

Wavelength (μm)	Slope ($\text{MJy sr}^{-1}/10^{20}\ \text{cm}^{-2}$)	Offset (MJy sr^{-1})	Offset without Outliers ^b (MJy sr^{-1})
100	0.62 ± 0.08	0.76 ± 0.37	0.71 ± 0.32
140	0.95 ± 0.17	1.11 ± 0.63	1.10 ± 0.52
240	0.72 ± 0.11	0.87 ± 0.55	0.83 ± 0.41

^a Mean and rms dispersion, from cell to cell.

^b Excluding those regions for which the slope deviates by more than 1.5 times its dispersion from its mean value.

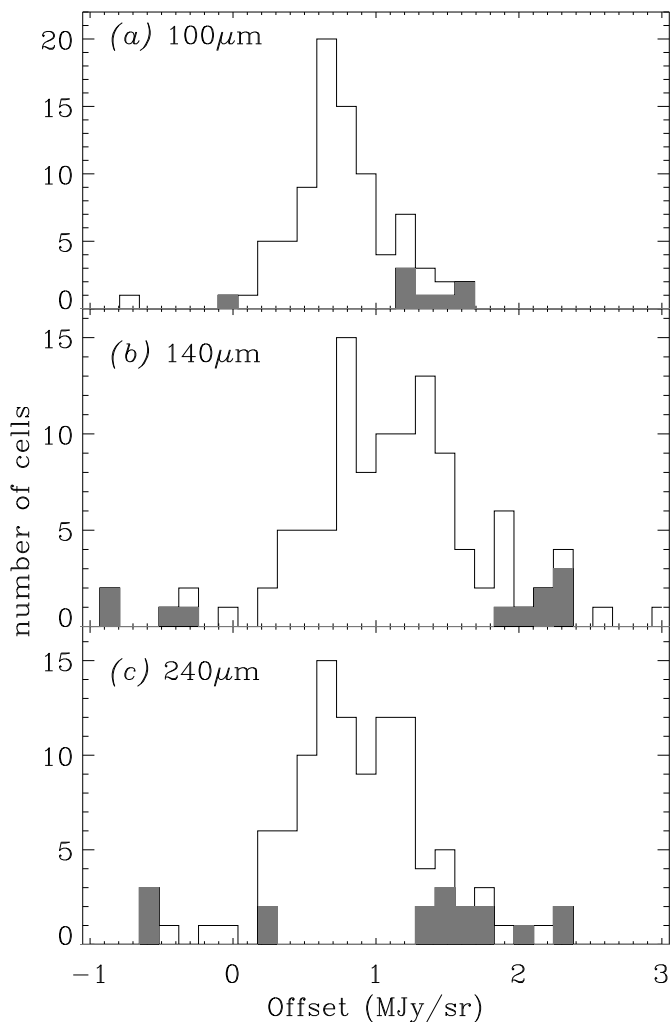


FIG. 4.—Similar to Fig. 3, but this time for the *offsets* of the infrared–H I correlations for sky patches with 10° radius. Each panel shows the results from a different DIRBE wave band: (a) $100\ \mu\text{m}$, (b) $140\ \mu\text{m}$, (c) $240\ \mu\text{m}$. The sky patches with outlying slope are shaded.

range of slopes and offsets. The *dispersion* of the putative infrared background brightnesses, listed in the last column of Table 2 precludes more than a $2\ \sigma$ (loosely speaking) confidence level detection of the infrared background, unless more restrictive assumptions about the galactic emission are made. The significance of this effect is discussed in more detail by Hauser et al. (1998) and Shafer et al. (1998). Fortunately, the separation of the galactic and cosmological contributions to the far-infrared sky brightness can be resolved using higher resolution and sensitivity far-infrared observations, such as have recently been performed with the *Infrared Space Observatory* (Kawara et al. 1997; Puget et al. 1998) and will eventually become possible with the NASA Space Infrared Telescope Facility and the ESA *Planck Surveyor*. These observations should reveal whether the brightness of the faintest parts of the sky is produced by an ensemble of extragalactic sources or by interstellar cirrus.

3. THE DISTRIBUTION OF INFRARED EXCESS

3.1. Definition of Infrared Excess

The infrared excess is defined to be the observed infrared surface brightness minus the contributions from dust

associated with the atomic interstellar medium, the zodiacal light, and the cosmic infrared background. We calculate the infrared excess using

$$I_v^{\text{ex}} = I_v - SN(\text{H I}) - O, \quad (2)$$

where S and O are the locally interpolated slope and offset of the infrared–H I correlation. The offset O contains residual zodiacal light and the cosmic infrared background and is not useful for measuring properties of the interstellar medium. We created infrared excess maps independently for the 100, 140, and $240\ \mu\text{m}$ wave bands, so that we can measure the far-infrared colors of the infrared excess.

The infrared excess map at $240\ \mu\text{m}$ is shown in an all-sky projection in Figure 5. The infrared excess is “patchy,” with significant structure on scales smaller than the size of the “cells” within which the infrared–H I slopes were determined. We have checked that the maps are not very different if the cell size is twice as large as the one we finally adopted.

The significance of a given value of the infrared excess can be determined statistically from its probability distribution. Figure 6 superposes the histograms of the positive and negative pixels in the infrared excess map. It is clear that the probability distribution is not random: *positive* values dominate negative values when $I_{100}^{\text{ex}} > 1\ \text{MJy sr}^{-1}$, which we will use as the lower limit to define infrared excess clouds. At the highest latitudes ($|b| > 45^\circ$) the dispersion is lower, so we use a threshold of $I_{100}^{\text{ex}} > 0.3\ \text{MJy sr}^{-1}$ to define clouds.

3.2. Atlas of Infrared Excess Clouds

A table of clouds would not suffice to describe the infrared excess, because the emission has some continuity over large scales. High-latitude molecular clouds have been shown to be associated with large H I features (Gir, Blitz, & Magnani 1994), suggesting their formation is related to events or processes (like supernovae and stellar winds) that organize the interstellar medium on large scales. For presentation here, and practical utility to other researchers, we present the infrared excess as an atlas consisting of eight maps with simple coordinate projections. We have preferred a Cartesian projection for latitudes $20^\circ < |b| < 50^\circ$, so that positions can be easily located with a ruler (Fig. 7). We also made maps of the two galactic polar caps, in a simple orthographic projection (Fig. 8). The maps we present here are for $100\ \mu\text{m}$ wavelength, the highest sensitivity of the DIRBE far-infrared wave bands. The maps at 140 and $240\ \mu\text{m}$ are generally similar. At $100\ \mu\text{m}$, there are more infrared excess clouds, because both *warmer than average* and *molecular* clouds produce infrared excess at $100\ \mu\text{m}$. However, the vast majority of structures in the far-infrared excess maps are shown in the next sections to be *cold*.

In order to study the properties of the “clouds” and regions of sky with infrared excess, we have identified two lists of positions and apertures within which to perform photometry. The first list is the catalog of previously known molecular clouds compiled by Magnani, Hartmann, & Speck (1997). (We combined entries that would be redundant at our low resolution.) These are indicated on the individual panels of the atlas. Second, we made a list of some of the remaining peaks in the infrared excess maps, with brightness comparable to the known molecular clouds. This list was created by hand, on inspection of both 100 and

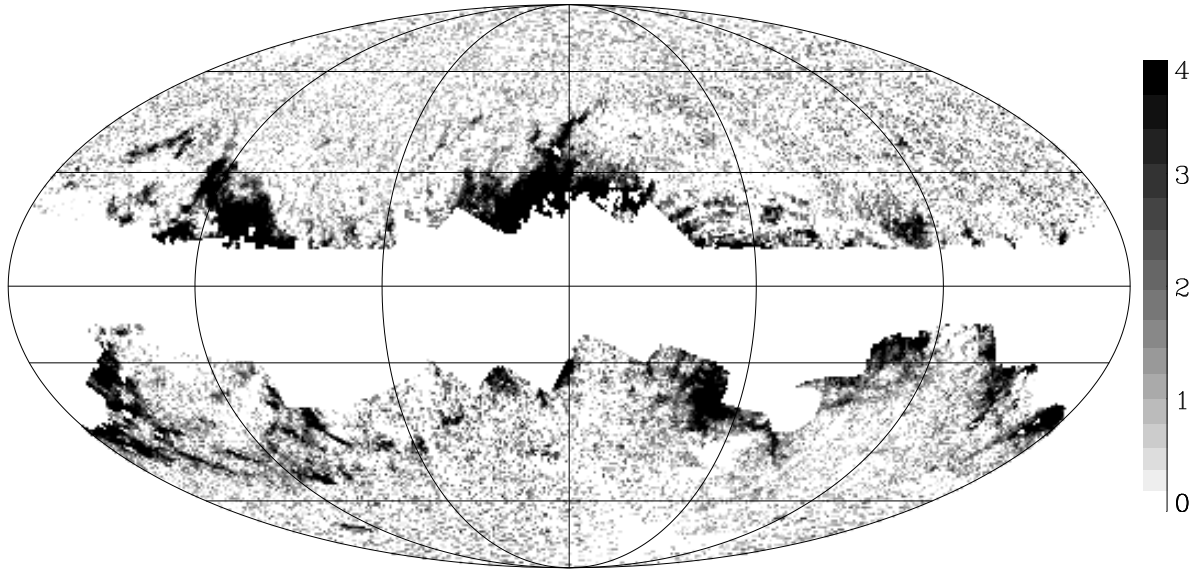


FIG. 5.—All-sky map of the residual $240\ \mu\text{m}$ surface brightness after subtracting the emission correlated with the H I column density. The map is shown in a galactic coordinate Mollweide projection as Fig. 2; meridians are drawn every 60° and parallels every 30° . The gray-scale range is illustrated by the bar, with units MJy sr^{-1} , to the right of the map.

$240\ \mu\text{m}$ infrared excess maps, and it is incomplete. The “new” clouds were named in the format $\text{DIR } lll \pm bb$ where lll is the galactic longitude and bb is the galactic latitude; the prefix “DIR” stands for “diffuse infrared” as in the name DIRBE. Third, for reference, we labeled many peaks in the infrared excess maps due to bright point sources, most of which are nearby galaxies (Odenwald, Newmark, & Smoot 1997).

The list of previously known clouds is shown in Table 3, and the newly identified clouds are shown in Table 4. For each cloud, we averaged the infrared excess surface brightness at 100 and $240\ \mu\text{m}$ within the cloud boundary. Only clouds detected at both 100 and $240\ \mu\text{m}$ are listed. The total infrared excess flux at $100\ \mu\text{m}$, the color temperature obtained from the $100/240\ \mu\text{m}$ ratio (assuming emissivity

proportional to v^2), and the approximate angular diameter of each cloud are shown in Tables 3 and 4.

The infrared excess clouds in general are relatively bright at $240\ \mu\text{m}$, and their far-infrared color temperature is significantly lower than that of average atomic clouds. This is illustrated in Figure 9, where histograms of the color temperatures of infrared clouds are shown. The fact that the vast majority of infrared excess clouds are *cold* confirms that the infrared excess is generally *not* due to clouds that are warmer than average. Indeed, because the clouds are colder than average, they tend to be underluminous in infrared emission. This effect has also been found by Lagache et al. (1998), who showed that molecular regions at high latitude can be identified by (1) deficiency in $60\ \mu\text{m}$ emission and (2) low $140/240\ \mu\text{m}$ color temperatures relative to atomic cirrus. One of the main uncertainties that has been faced by past studies of infrared excess as a tracer of molecular gas (e.g., Désert et al. 1988; Reach et al. 1994) was the uncertainty as to whether the infrared surface brightness at $60\ \mu\text{m}$, observed by *IRAS* and often compared to the $100\ \mu\text{m}$ brightness, traces variations in column density or dust temperature. By use of the *COBE* observations at $240\ \mu\text{m}$, this problem has now been resolved.

3.3. Warm Infrared Excess Clouds

While they are rare, there are some infrared excess clouds that are *warmer* than average. The single most prominent example is the large H II region around the nearby B star α Vir, or Spica, which was first discovered by its extensive $\text{H}\alpha$ emission (Reynolds 1985). The Spica H II region is exceptional in that it is produced by one of the closest—at $d = 80 \pm 5\ \text{pc}$ (ESA 1997)—early-type stars; it is at high galactic latitude, where it can be easily separated from other sources; and the star is presently in a region of relatively low interstellar medium density, so that its H II region covers a region some 15° across. The dust in the Spica H II region is significantly warmer than typical interstellar cirrus, and it is unusual in that it also has 12 and $25\ \mu\text{m}$ emission significantly higher than expected from the 100 –

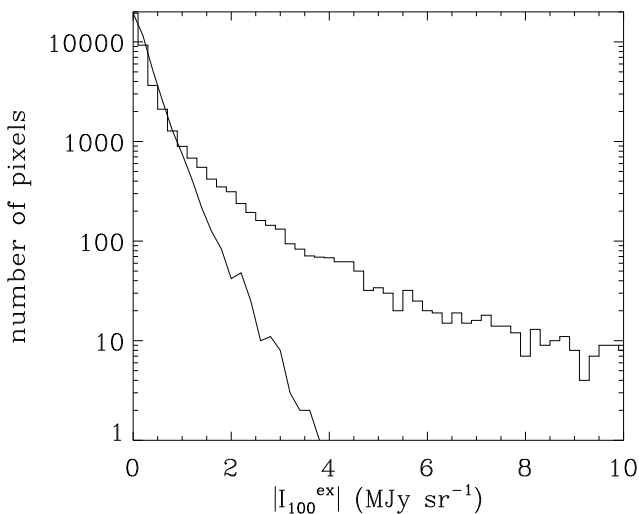


FIG. 6.—Histograms of the infrared excess at $100\ \mu\text{m}$. The upper histogram shows the distribution of the positive values of infrared excess, and the curve beneath it shows the distribution of the negative values. The positive values clearly dominate above an infrared excess of $1\ \text{MJy sr}^{-1}$.

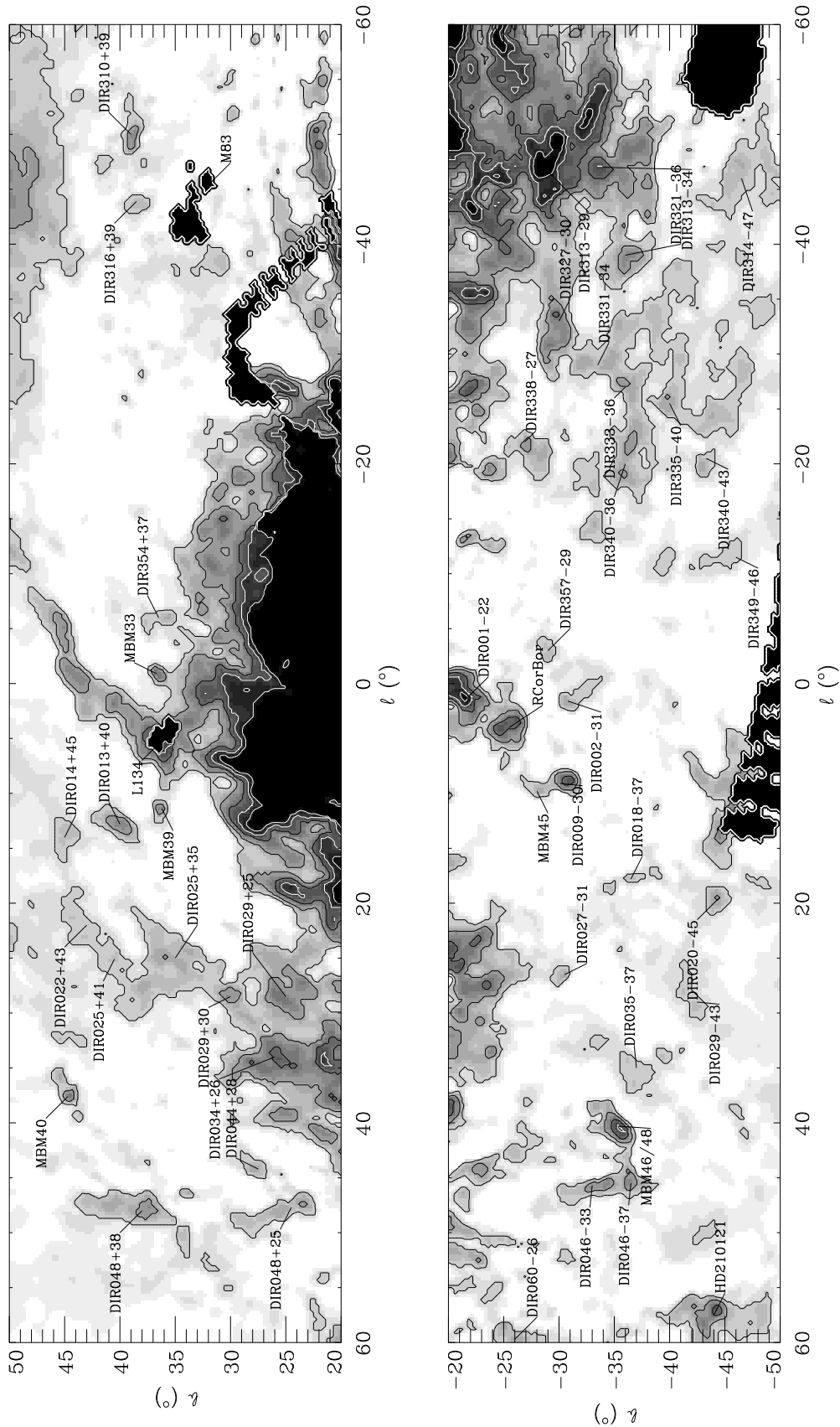


FIG. 7a

FIG. 7.—Atlas of the $100\ \mu\text{m}$ infrared excess in galactic coordinate Cartesian projections, for absolute galactic latitudes 20° – 50° of longitude, with the centers at longitudes 0° (a), 120° (b), and 240° (c). The upper part of each panel shows positive galactic latitudes, and the lower part shows negative galactic latitudes. In each panel, the most significant clouds are identified and labeled using the catalog of Magnani et al. (1996) or, for new clouds, the “DIR III \pm bb ” cloud name. The gray scale ranges from -0.2 (white) to 5 (black) MJy sr^{-1} at $100\ \mu\text{m}$ wavelength. Contours are drawn at 0.3, 1, 2, 3, and $4\ \text{MJy sr}^{-1}$ (but the highest levels are not present in every map). The large black areas are masked, either because of lack of HI data, presence of the Magellanic Clouds, or presence of extremely bright and structured infrared emission.

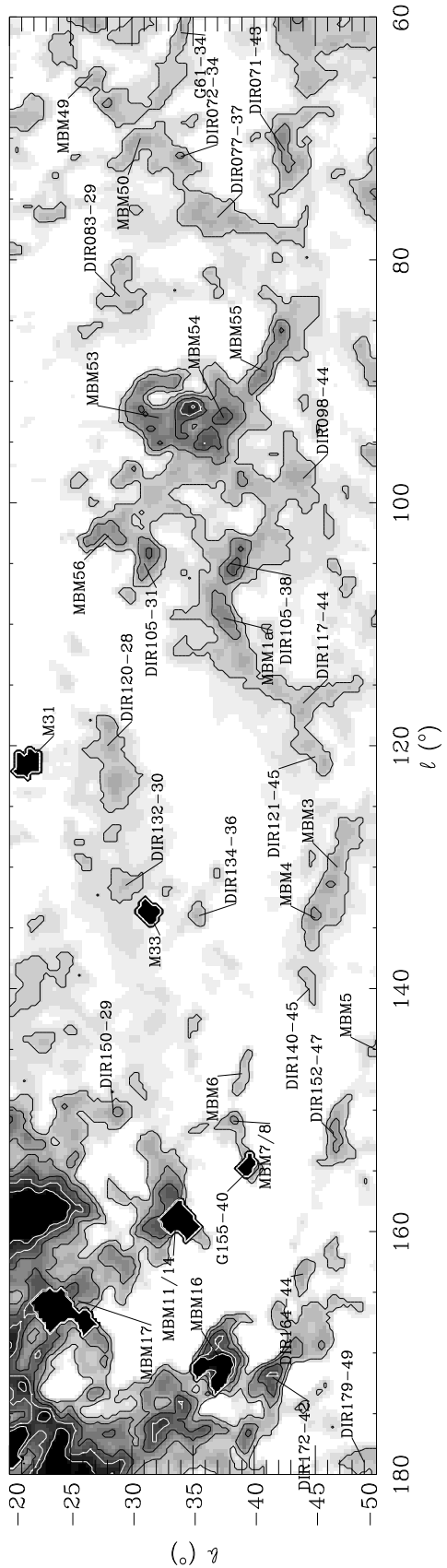
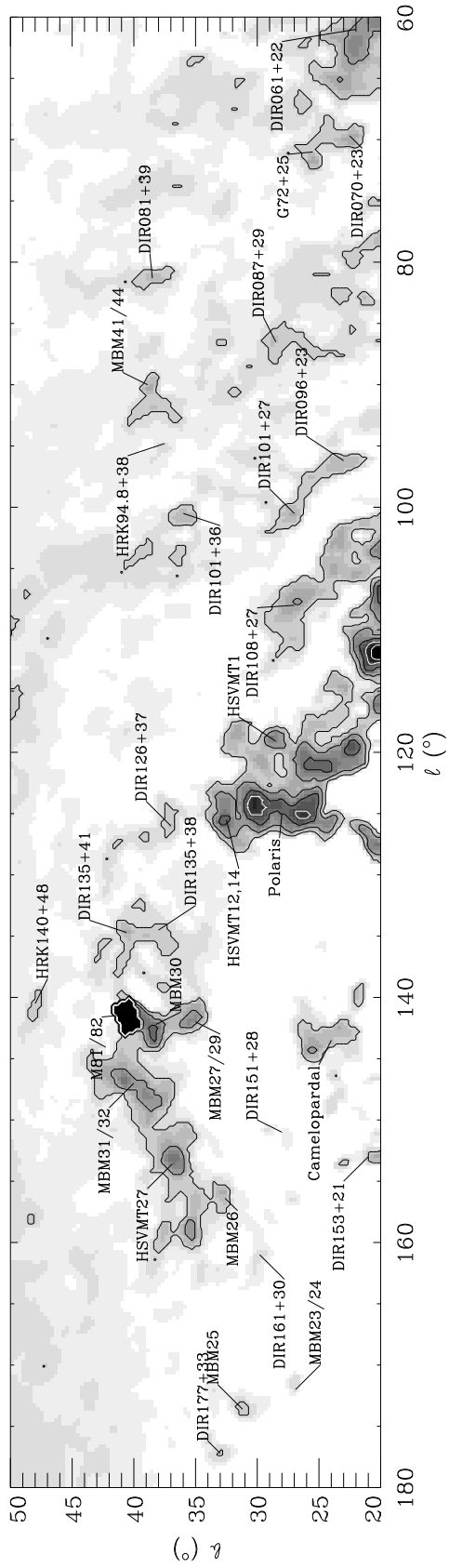


FIG. 7b

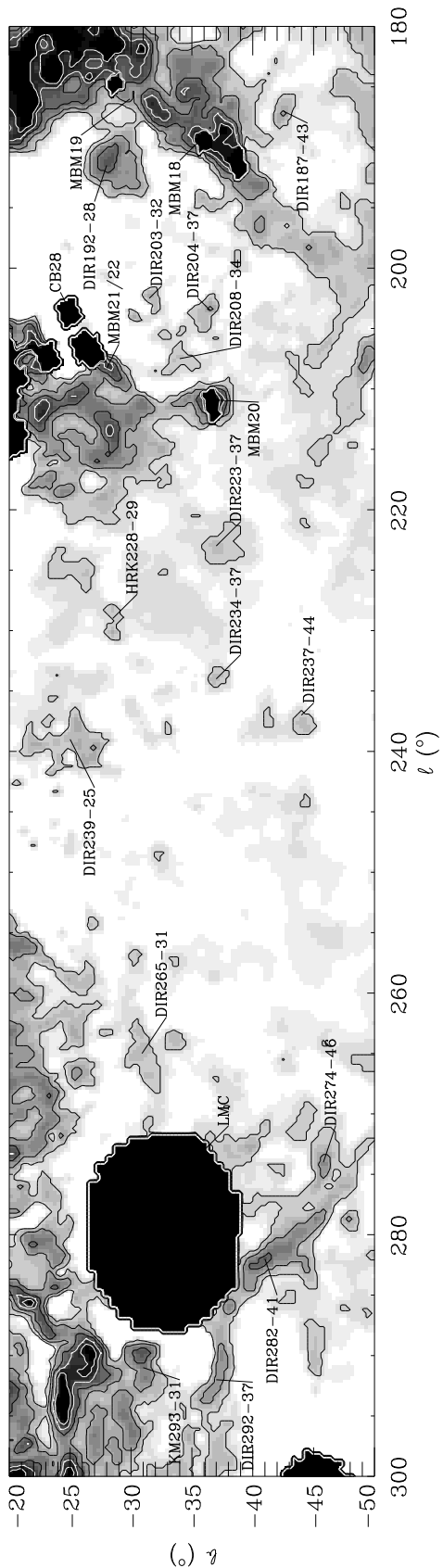
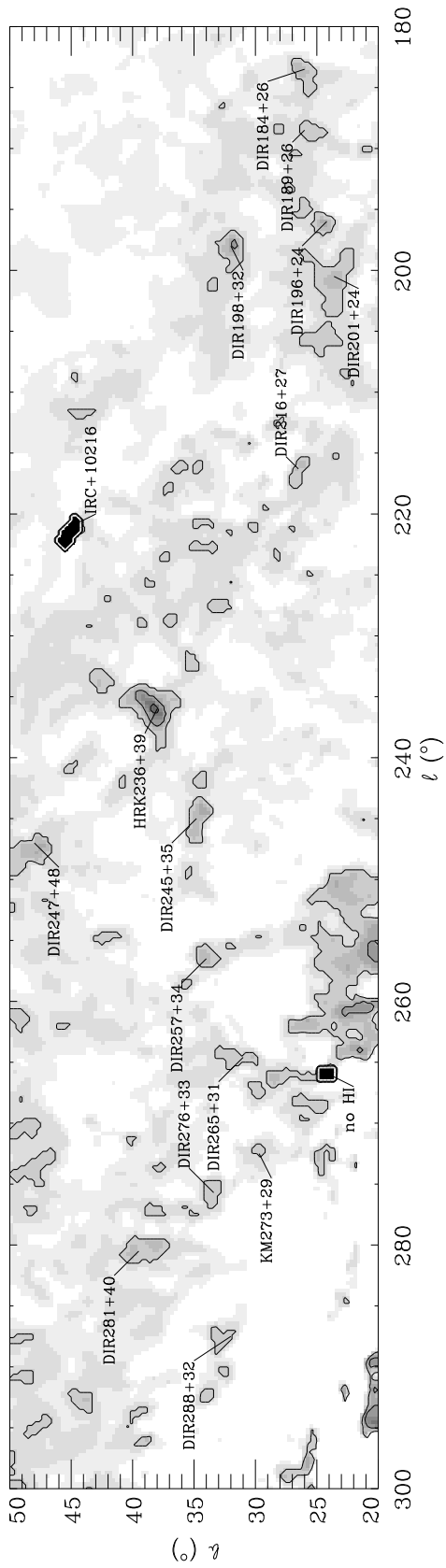


FIG. 7c

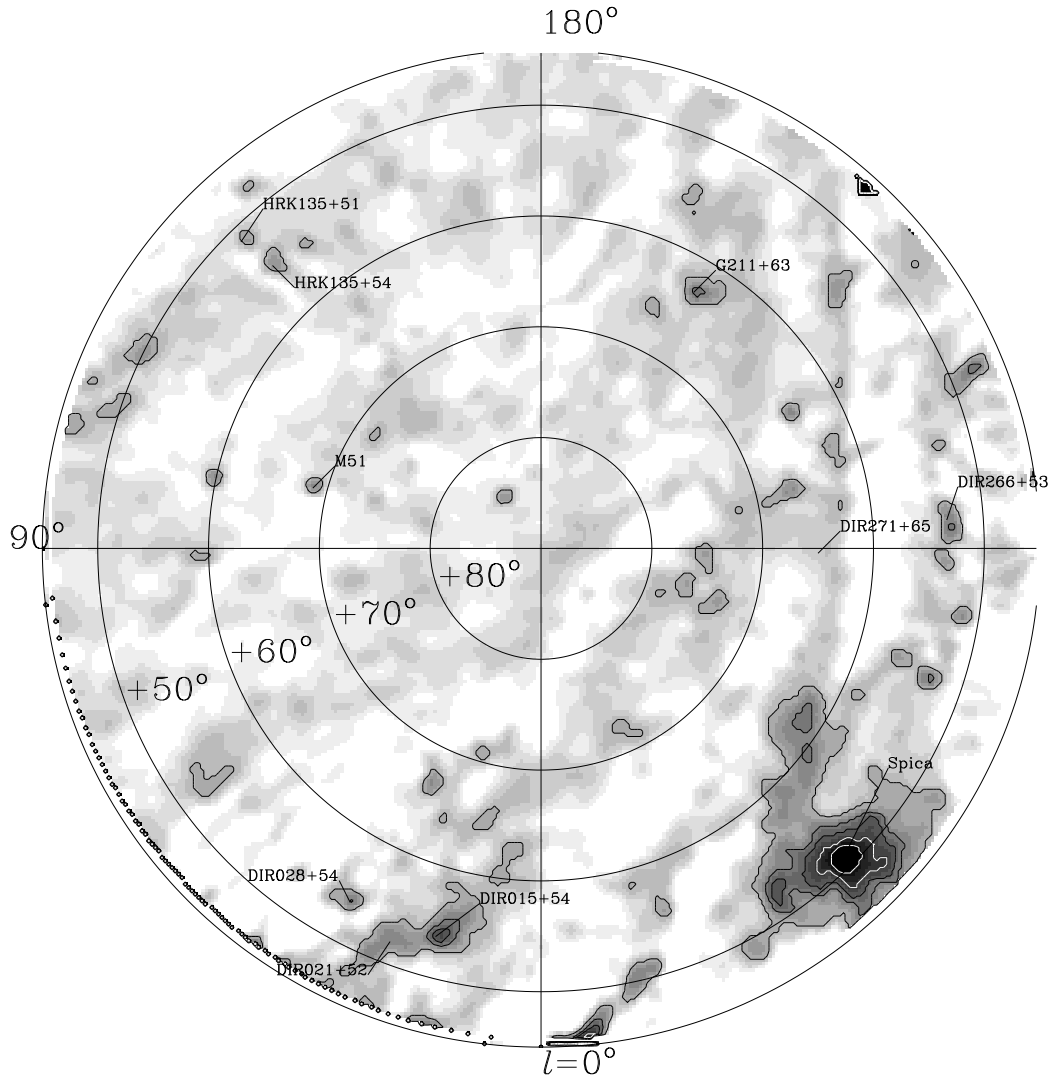


FIG. 8a

FIG. 8.—Maps of the $100\ \mu\text{m}$ infrared excess at the galactic poles, in orthographic projections. Panel *a* covers the north Galactic pole and panel *b* covers the south Galactic pole. As in the previous figure, the most significant infrared excess clouds are labeled. The gray-scale range, from white to black, is -0.2 to $3\ \text{MJy sr}^{-1}$. Contours are drawn at $0.1, 1, 0.5, 1,$ and $2\ \text{MJy sr}^{-1}$. (The contours are at lower values in this figure than in Fig. 7, in order to bring out fainter features near the poles.) The large black stripe in panel *b* is due to a region where the H I 21 cm data are poorly sampled.

$240\ \mu\text{m}$ emission, suggesting a modified grain size distribution (Zagury 1997). There are no other “warm” infrared excess clouds comparable to the Spica H II region in size and brightness, most likely because no other early-type star is as advantageously situated.

One significant “warm” infrared excess cloud that has not been noted before is DIR 015 + 54. This is one of the brightest $60\text{--}100\ \mu\text{m}$ infrared excess clouds at high positive galactic latitudes (Fig. 8a), but it is not detected at $240\ \mu\text{m}$ (and therefore is absent from Table 4). In order to see the structure of this cloud at higher angular resolution, we extracted *IRAS* images at $12, 25, 60,$ and $100\ \mu\text{m}$ from the *IRAS* Sky Survey Atlas (ISSA); the ISSA $60\ \mu\text{m}$ image is shown in Figure 10. The local background-subtracted surface brightness at $60\ \mu\text{m}$, averaged over the central $30'$, is $0.8\ \text{MJy sr}^{-1}$, and the ratio of $60/100\ \mu\text{m}$ brightnesses is 0.46 , a factor of 2 higher than that of atomic “cirrus” and much higher than that of molecular clouds. The cloud color and shape are similar to a bow shock (van Buren & McCray

1988) produced by an object moving toward the northeast. However, there is no nearby early-type star—which would be very bright at visible wavelengths owing to the low extinction along the line of sight—that could plausibly create this nebula, either as an H II region or a bow shock. The nature of the brightest pointlike $60\ \mu\text{m}$ emission, which is listed in the *IRAS* Faint Source Catalog as F15101 + 1206 (Moshir et al. 1989), is unknown, although statistically it is likely to be extragalactic (Reach, Heiles, & Koo 1993).

We find that there is a faint optical counterpart of F15101 + 1206 in the Palomar Observatory Sky Survey,² consistent with the idea that F15101 + 1206 is extragalactic.

² Based on photographic data of the National Geographic Society–Palomar Observatory Sky Survey (NGS-POSS) obtained using the Oschin Telescope on Palomar Mountain. The NGS-POSS was funded by a grant from the National Geographic Society to the California Institute of Technology. The plates were processed into the present compressed digital form with their permission. The Digitized Sky Survey was produced at the Space Telescope Science Institute under US Government grant NAG W-2166.

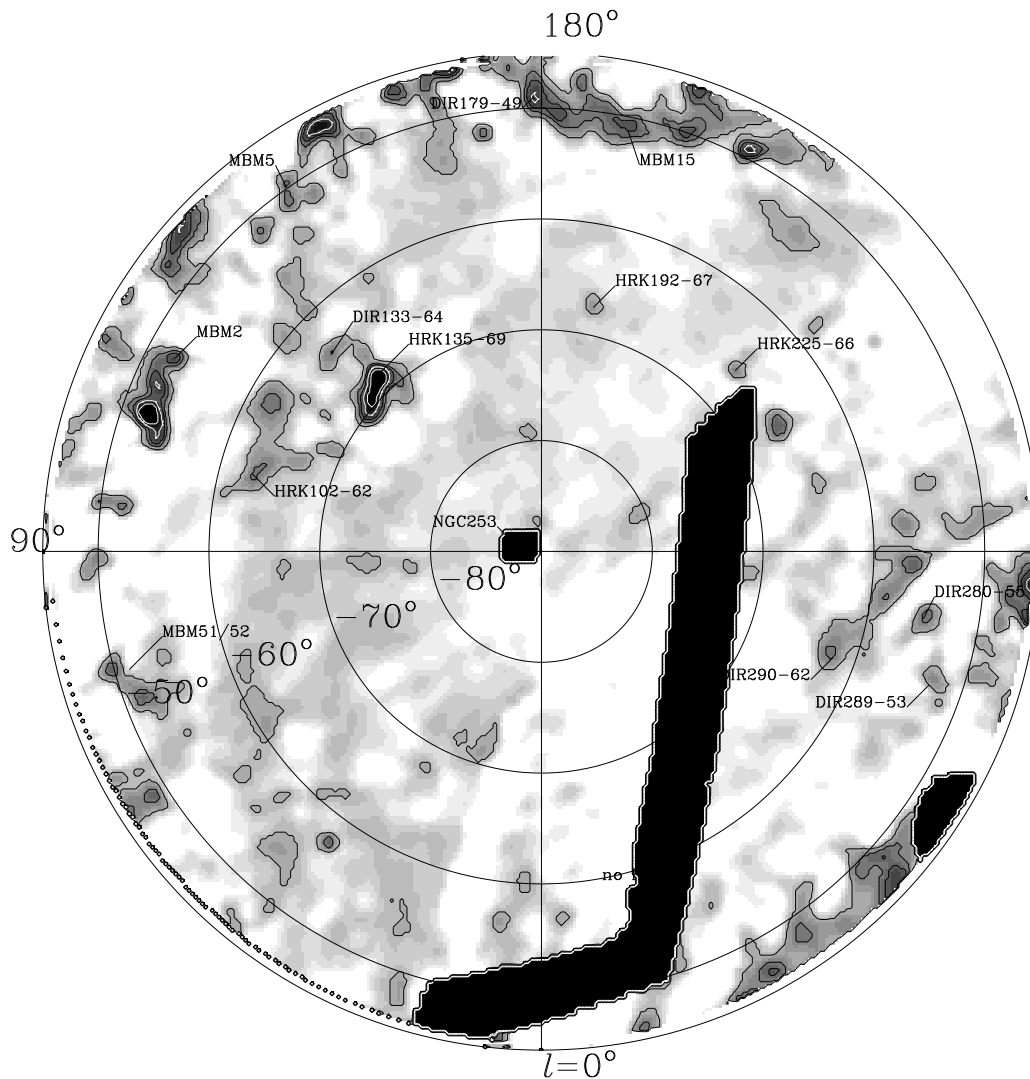


FIG. 8b

There is no optical counterpart for the diffuse emission of DIR 015 + 54.

The infrared colors of DIR 015 + 54 are similar to those of the nearby galaxy NGC 6822 (Israel et al. 1996), suggesting perhaps that the cloud could in fact be another low surface brightness member of the Local Group. We inspected the individual H I spectra from the Leiden-Dwingeloo 21 cm line survey near this position, and we find that the cloud is clearly present, with a “normal” LSR velocity of -17 km s^{-1} and both narrow and wide line components (dispersions 3 and 15 km s^{-1} , respectively). We suspect therefore that DIR 015 + 54 is a Galactic cloud that happens to be somewhat brighter than average in the far-infrared and much brighter than average at $60 \mu\text{m}$. The high $60 \mu\text{m}$ brightness of this cloud may be due to a significantly enhanced population of small grains, which argues that dust properties can vary widely from cloud to cloud.

3.4. Infrared Excess and Molecular Gas

3.4.1. Comparison with Known Molecular Clouds

Our atlas of infrared excess clouds reveals essentially *all* previously known high-latitude molecular clouds in the literature (Magnani et al. 1996). First, consider the clouds

originally found by Magnani, Blitz, & Mundy (1985, hereafter MBM); these clouds were first identified as regions of extinction on the Palomar Observatory Sky Survey plates, and then they were detected in CO ($J = 1 \rightarrow 0$) emission with radio telescopes. At our low angular resolution, the MBM clouds are made up of essentially 36 individual regions. Of these, well-formed clouds with significant infrared excess ($I_{100}^{\text{ex}} > 1 \text{ MJy sr}^{-1}$) were clearly detected from 34 regions, for a 94% detection rate. MBM 19 and MBM 9, the two regions for which we do not see an infrared “cloud,” both are in regions of significant infrared excess, but there is no well-defined cloud at their position. Indeed, this is somewhat true of some of the other clouds as well: the center of the infrared excess region does not coincide with the center of the MBM cloud. We suspect that the MBM positions are relatively dense cores (with well-defined extinction on the optical plates), while the overall cloud structure is better represented by the infrared excess map.

Our atlas of infrared excess is significantly different from the catalog of 515 infrared excess clouds obtained by Désert et al. (1988, hereafter DBB). We have attempted to associate each entry of Tables 3 and 4 with a cloud in the DBB catalog. For 62% of the MBM clouds, we find corresponding entries in the DBB catalog. This is somewhat higher

TABLE 3

INFRARED EXCESS FROM KNOWN HIGH-LATITUDE MOLECULAR CLOUDS

Name ^a	<i>l</i>	<i>b</i>	Size (deg)	<i>T</i> (240/100) ^b (K)	<i>F</i> ₁₀₀ ^{ex b} (kJy)
DC001.4-21.6	1.4	-21.6	0.6	16.2	1.31
R Cor Bor	4.0	-25.5	2.0	17.1	...
LDN 134.....	5.0	36.0	3.0	14.8	...
MBM 45	9.8	-28.0	1.0	14.2	0.72
MBM 39	11.4	36.2	1.9	16.6	1.56
MBM 40	37.6	44.7	2.2	15.9	0.48
MBM 46/48	40.3	-35.3	2.0	16.9	2.12
HD 210121	57.5	-44.0	4.0	16.3	3.57
G61-34	61.3	-34.0	1.3	15.2	1.16
MBM 49	64.7	-26.8	1.0
MBM 50	70.0	-30.7	5.5	21.0	1.85
G72+25	71.0	25.5	1.0	17.7	...
MBM 51/52	74.0	-51.3	4.0	17.0	0.66
MBM 55	89.2	-40.9	3.4	14.6	1.77
MBM 41/44	90.0	38.9	1.8	15.7	...
MBM 53	93.0	-32.2	4.4	19.0	...
MBM 54	93.0	-37.5	4.3	15.9	...
HRK 94.8+38	94.8	37.5	1.2
MBM 56	102.7	-28.1	2.5	17.2	1.24
MBM 1	110.2	-41.2	0.5	17.8	0.57
MBM 2	117.7	-52.6	1.9	19.0	1.28
HSVMT 1	119.1	28.5	1.8	15.9	0.61
Polaris.....	125.0	28.0	5.0	15.1	0.79
HSVMT 12/14	125.5	32.5	1.0	16.0	0.33
MBM 3	130.0	-46.8	2.5	15.4	1.21
MBM 4	134.2	-45.0	2.0	14.7	0.63
HRK 135+51	135.6	51.3	1.5	16.2	0.62
HRK 135-69	136.4	-68.3	1.8	17.9	2.32
HRK 135+54	136.5	54.8	1.1	17.5	2.86
HRK 140+48	140.5	48.0	0.7	24.4	0.74
MBM 27/29	142.0	35.0	2.2	15.6	...
MBM 30	142.2	38.2	3.4	15.2	0.50
Camelopardalis.....	143.5	24.0	2.9	16.0	0.61
MBM 5	145.0	-49.9	3.8	13.8	0.60
MBM 6	147.0	-39.0	1.9	15.0	1.07
MBM 31/32	147.0	40.0	4.2	15.9	...
MBM 7/8	150.9	-38.3	1.5	14.8	2.87
HSVMT 27	153.6	36.9	2.8	15.7	2.20
G155-40	154.7	-39.8	1.4	15.2	0.91
MBM 26	156.4	32.6	2.0	18.1	...
MBM 11/14	159.0	-33.6	3.5	15.3	0.62
MBM 17	165.7	-25.6	0.5
MBM 16	171.2	-37.7	0.5	15.5	0.77
MBM 23/24	172.0	26.9	0.8	15.5	0.84
MBM 25	173.6	31.2	2.0	15.9	...
MBM 19	186.0	-29.9	0.5
MBM 18	189.1	-36.0	0.5
MBM 15	191.7	-51.3	3.5	17.7	...
HRK 192-67	192.0	-67.5	1.4	18.5	2.29
CB 28	204.0	-25.2	1.5	14.9	0.28
MBM 21-22.....	208.3	-28.0	2.0	19.6	0.53
G211+63	210.8	63.1	2.0	18.4	...
MBM 20	210.9	-36.5	2.5	15.4	2.27
HRK 225-66	227.0	-66.1	2.5	15.6	2.69
HRK 228-29	229.0	-28.5	1.7	16.4	...
HRK 236+39	236.0	38.0	4.0	16.5	0.22
KM 273+29	272.5	29.7	2.0	17.9	0.65
KM 293-31	291.0	-31.0	2.2
KM 300-24	301.1	-24.5	2.0
MBM 33	359.1	36.7	1.2	15.7	...

^a Cloud names mostly from the compilation of high-latitude molecular clouds (Magnani et al. 1996). MBM: extinction patches on Palomar Observatory Sky Survey (Magnani et al. 1985), KM, DC: extinction patches in European Southern Observatory sky survey (Keto & Myers 1986; Hartley et al. 1986), HRK: infrared cirrus patches in IRAS 100 μ m maps (Heiles et al. 1988).

^b Values listed as “...” in clouds for which the COBE/DIRBE data indicate strong, unresolved structure (consistent with a bright point source.)

TABLE 4

CATALOG OF UNIDENTIFIED INFRARED EXCESS CLOUDS

Name	<i>l</i>	<i>b</i>	Size (deg)	<i>T</i> (240/100) (K)	<i>F</i> ₁₀₀ ^{ex} (kJy)
DIR 002+31	1.6	-30.8	1.2	18.4	0.89
DIR 009+30.....	9.1	-30.1	2.3	16.5	2.50
DIR 013+40.....	12.8	40.0	1.5	17.1	1.31
DIR 018+37.....	17.8	-36.5	2.5	12.2	0.04
DIR 020+45.....	19.5	-44.5	1.7	18.9	0.69
DIR 021+52.....	21.0	52.0	1.5	17.5	0.29
DIR 025+35.....	25.0	35.0	3.5	21.8	2.96
DIR 027+31.....	26.5	-30.5	1.0	15.3	0.52
DIR 028+54.....	28.3	53.7	1.0	17.3	0.29
DIR 029+25.....	28.5	25.0	2.6	16.6	2.15
DIR 029+30.....	28.5	30.0	1.1	16.7	0.72
DIR 034+26.....	34.0	26.0	3.0	18.6	3.21
DIR 046+37.....	45.5	-36.5	1.6	16.1	1.24
DIR 046+33.....	45.7	-33.0	2.2	22.4	0.72
DIR 048+25.....	47.7	24.5	2.1	16.9	1.49
DIR 048+38.....	48.0	38.0	2.5	18.0	1.56
DIR 060+26.....	59.7	-26.0	1.7	22.3	1.07
DIR 061+22.....	61.0	22.0	4.0	26.1	3.57
DIR 070+23.....	69.7	22.5	1.2	17.2	0.63
DIR 071+43.....	71.0	-42.5	3.0	15.5	3.14
DIR 072+34.....	71.5	-34.0	1.4	15.9	0.43
DIR 077+37.....	76.5	-37.0	3.3	18.5	1.75
DIR 081+39.....	81.3	38.5	2.5	16.2	0.80
DIR 087+29.....	86.5	28.5	3.5	23.1	1.07
DIR 096+23.....	96.2	23.0	2.0	19.3	1.17
DIR 098+44.....	98.0	-44.0	2.5	17.4	0.97
DIR 105-31.....	105.0	-31.0	1.8	15.3	1.16
DIR 105-38.....	105.0	-38.0	2.7	15.7	2.48
DIR 108-27.....	108.0	27.0	2.7	18.1	2.12
DIR 117-44.....	116.5	-44.0	2.0	18.0	0.70
DIR 120-28.....	120.0	-28.0	2.4	17.7	1.28
DIR 121-45.....	120.9	-45.0	1.8	15.5	0.57
DIR 126-37.....	126.0	37.0	0.9	16.7	0.30
DIR 132-30.....	131.5	-29.5	1.9	18.4	0.61
DIR 134-36.....	134.0	-35.5	1.5	16.3	0.62
DIR 135-38.....	134.5	38.0	1.4	23.4	0.28
DIR 135-41.....	134.7	40.6	1.4	17.0	0.34
DIR 140-45.....	140.0	-44.5	2.0	19.8	0.63
DIR 150-29.....	150.2	-28.5	1.7	16.2	0.89
DIR 152-47.....	152.0	-46.5	3.0	16.2	2.74
DIR 164-44.....	163.5	-44.0	1.6	17.0	0.61
DIR 172-42.....	172.0	-41.5	2.3	15.6	2.87
DIR 177-33.....	177.2	33.0	1.5	16.3	0.56
DIR 179-49.....	179.0	-49.0	3.5	20.4	1.68
DIR 184-26.....	183.5	26.0	1.8	17.8	0.66
DIR 187-43.....	187.0	-42.5	1.7	20.4	0.58
DIR 196-24.....	196.0	24.2	1.0	17.2	0.46
DIR 198-32.....	198.0	32.0	1.5	15.8	0.61
DIR 201-24.....	200.5	23.6	1.3	19.9	0.39
DIR 203-32.....	202.5	-31.5	2.0	14.9	0.33
DIR 204-37.....	203.5	-36.5	1.8	15.6	0.79
DIR 216+27.....	216.3	26.5	2.2	16.2	0.34
DIR 223+37.....	223.0	-37.0	2.7	22.3	1.21
DIR 234+37.....	234.0	-37.0	1.1	21.2	0.65
DIR 237+44.....	237.0	-44.0	1.2	19.7	0.72
DIR 239-25.....	239.0	-25.0	4.0	20.5	3.34
DIR 245+35.....	245.0	34.8	2.1	17.1	0.88
DIR 257+34.....	256.5	34.0	1.5	16.2	0.76
DIR 265+31.....	265.0	-30.9	3.0	16.2	1.96
DIR 274+46.....	274.0	-45.8	1.4	18.1	0.63
DIR 276+33.....	275.7	33.4	1.2	18.4	0.52
DIR 280+55.....	280.0	-55.0	3.1	17.0	0.91
DIR 281-40.....	280.5	39.5	2.0	23.6	0.48
DIR 282+41.....	282.0	-41.0	4.0	17.6	3.42
DIR 288+32.....	287.5	32.0	3.0	18.5	2.12
DIR 289-53.....	289.0	-53.0	3.5	16.2	0.95
DIR 290-62.....	290.0	-62.0	4.5	18.3	2.20
DIR 292-37.....	292.0	-37.0	3.0	17.7	2.71
DIR 310+39.....	310.0	39.0	1.9	16.8	0.99
DIR 313-34.....	313.0	-34.0	1.5	18.1	0.62
DIR 314-47.....	314.0	-46.5	4.4	19.8	2.76
DIR 316+39.....	316.1	38.5	1.4	18.6	0.61

TABLE 4—Continued

Name	l	b	Size (deg)	$T(240/100)$ (K)	F_{100}^{ex} (kJy)
DIR 321+36.....	321.0	-36.0	2.5	19.2	2.32
DIR 327+30.....	327.0	-30.0	3.0	17.6	2.86
DIR 331-34.....	331.0	-33.5	2.1	21.4	0.69
DIR 333+36.....	333.0	-36.0	1.9	17.0	0.74
DIR 335-40.....	334.5	-40.0	1.3	19.1	0.71
DIR 340-43.....	339.5	-43.3	1.4	16.0	0.50
DIR 349-46.....	348.5	-46.0	1.9	20.1	0.93
DIR 354-37.....	354.0	36.5	1.6	17.8	0.72
DIR 357-29.....	357.0	-29.0	1.3	15.7	0.60

than the 47% detection rate determined by DBB, because of the way we grouped MBM clouds into complexes and considered a match if the DBB and MBM positions fall within the same cloud in Figures 7 or 8. Specifically, this means we consider the MBM clouds to be much larger than the high-extinction and CO-emitting cores. The higher detection rate of MBM clouds in our atlas is due to the higher quality input data that we used; both the infrared and H I data are of substantially higher quality than the data available to DBB. Many of the clouds that are not listed in DBB are very bright in our atlas, including both well-known (MBM) and new clouds. On the other hand, a significant fraction of DBB clouds are not confirmed by the present analysis. In

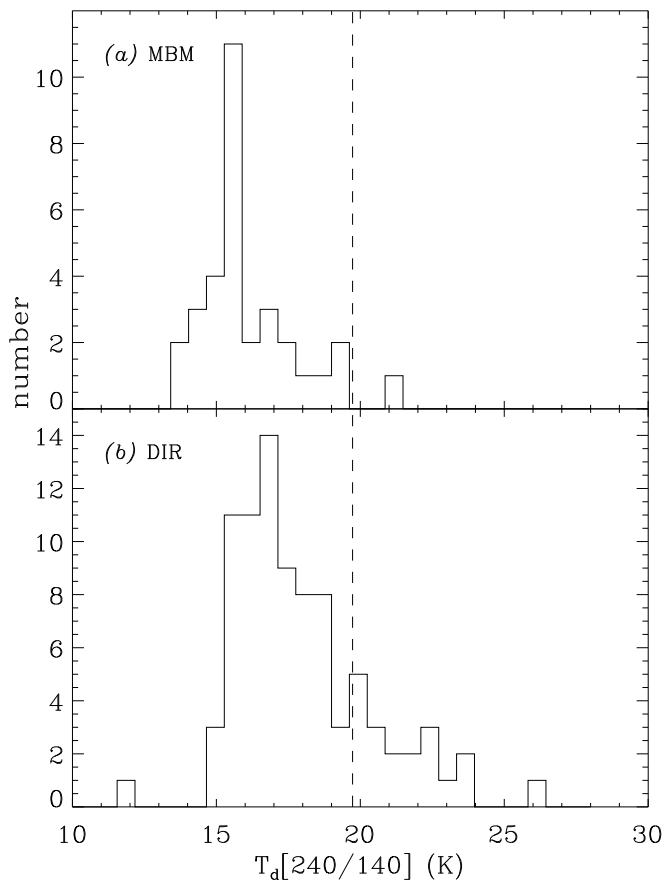


FIG. 9.—Histograms of color temperatures of MBM clouds (*top*) and DIRBE clouds (*bottom*) obtained from the infrared excess at 100 and 240 μm . The color temperature of emission associated with the atomic gas is shown as a dashed line. Both the MBM clouds, which are known to be molecular, and the new infrared excess clouds are colder than atomic clouds, most likely because they are optically thick to the high-energy part of the interstellar radiation field.

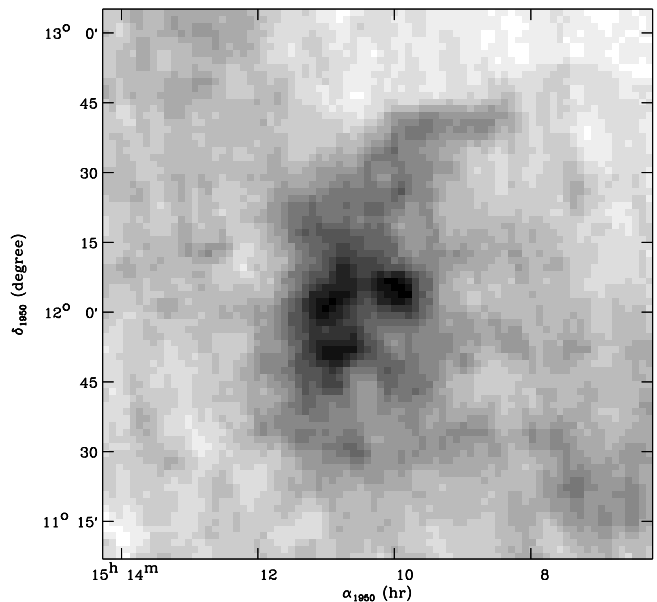


FIG. 10.—Surface brightness map at 60 μm of the warm infrared excess cloud DIR 015+54, made from the IRAS Sky Survey Atlas. The minimum surface brightness in the map is $-1.83 \text{ MJy sr}^{-1}$ (negative because of oversubtraction of zodiacal light), and the contours are at -1.35 , -1 , and $-0.65 \text{ MJy sr}^{-1}$.

total, we find counterparts for 45% of the DBB clouds and hints for another 7%, leaving 48% with no evident infrared excess in our maps. Of the unconfirmed clouds, 58% have a “significance” criterion less than 5 listed in the DBB table, but 10% (mostly H I artifacts) are listed with significance greater than 7. The uncertainties in the infrared excess method—especially with the lower quality infrared and H I data used by DBB, but also with the results presented in this paper—are dominated by systematic uncertainties rather than random noise. We have therefore chosen to make a relatively short table of 81 selected clouds and to present the skymaps for use by others.

3.4.2. Comparison with CO Observations in Ursa Major-Ursa Minor-Camelopardalis

The interstellar medium is not an ensemble of clouds with well-defined boundaries; it is coherent over large angular scales. Therefore, a comparison of cloud catalogs can be misleading. There are few regions where the CO ($J = 1 \rightarrow 0$) line has been mapped in emission on scales large enough to make a meaningful comparison with our atlas. The largest scale high-latitude CO map of which we are aware was made with a 1.2 m telescope, whose large beam ($9'$) is well suited to comparison with our results. A large portion of the Ursa Minor-Ursa Major region has been covered in a number of surveys, including one very large, regularly sampled grid (Heithausen et al. 1993). We have projected our infrared excess map onto the grid of the CO map assembled by Heithausen et al. (1993) for detailed comparison—see Figure 11. The agreement between the contour of integrated CO line brightness, $W(\text{CO})$, and the infrared excess contour is remarkably good, and the infrared excess map contains no significant clouds in regions without CO. Figure 12 shows a pixel-by-pixel scatter diagram for these maps. A linear fit of the infrared excess to the CO line integral, taking into account statistical uncertainties of 0.5 K km s^{-1} in $W(\text{CO})$ and 0.3 MJy sr^{-1} in I_{100}^{ex}

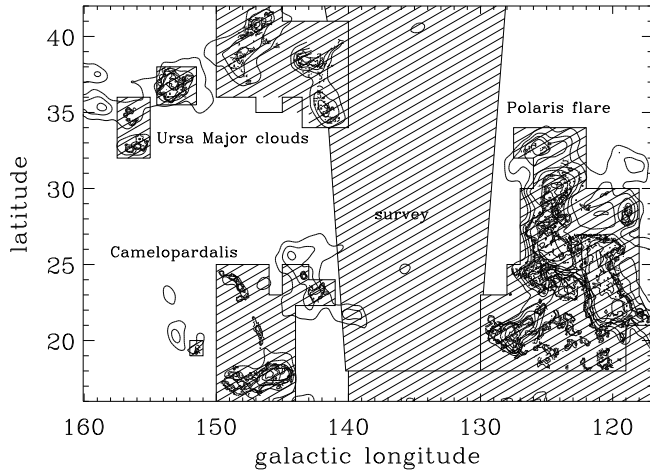


FIG. 11.—Comparison of the infrared excess (*smooth contours*) and CO (1 → 0) line integral for the Ursa Major-Ursa Minor-Camelopardalis region. Regions where the CO was observed are surrounded by thick lines and filled with thin diagonal lines. The two maps are in very good agreement where data for both maps exist. The infrared excess predicts, accurately, the location and extent of the molecular clouds. Furthermore, there are no “extra” infrared excess clouds predicted in the regions where CO was observed but not detected.

yields the following:

$$W(\text{CO}) = (-0.19 \pm 0.05) + (1.17 \pm 0.05) \times (I_{100}^{\text{ex}}/\text{MJy sr}^{-1}) \text{ K km s}^{-1}. \quad (3)$$

At low H I column densities, the correlation of *total* galactic 100 μm emission with H I column density in this region (which largely overlaps with that shown in Fig. 1) yields

$$I_{100} = 0.47 \pm 0.1 + (0.62 \pm 0.03) \times [N(\text{H I})/10^{20} \text{ cm}^{-2}] \text{ MJy sr}^{-1}. \quad (4)$$

If the infrared emission per H nucleus were the same in atomic and molecular gas, then we find that the H_2 column density per unit-integrated CO (1 → 0) line brightness is

$$X_{\text{naive}} = N(\text{H}_2)/W(\text{CO}) = (0.7 \pm 0.1) \times 10^{20} \text{ cm}^{-2} \text{ K}^{-1} \text{ km}^{-1} \text{ s}, \quad (5)$$

where the subscript “naive” is explained in the next paragraph.

We can determine the separate emissivities of the atomic and molecular gas using a multiple linear regression between the infrared, H I, and CO surface maps over the parts of the region that have been observed at all three wavelengths—assuming the H I and CO maps are sufficiently orthogonal. Table 5 shows the slopes from fits of the form

$$I_\nu = aN(\text{H I}) + bW(\text{CO}) + c \quad (6)$$

for several infrared wavelengths. It is evident that a and b

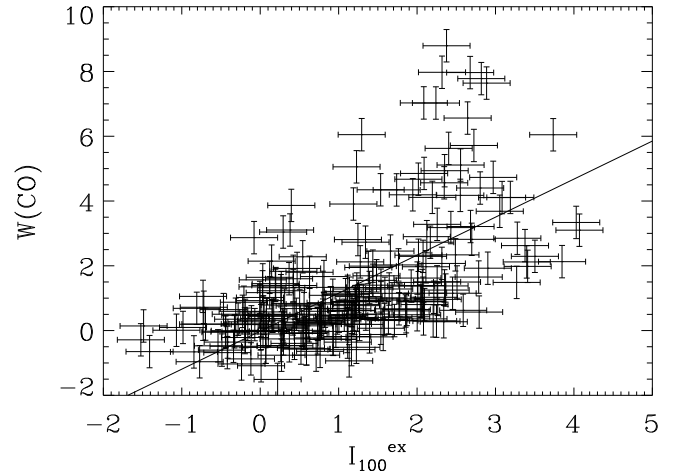


FIG. 12.—Correlation of the infrared excess, I_{100}^{ex} (MJy sr^{-1}), and CO (1 → 0) line integral, $W(\text{CO})$ (K km s^{-1}) for the north celestial pole region. Each point corresponds to an independent $40' \times 40'$ pixel.

depend on wavelength differently and the interpretation is straightforward: the dust mixed with the atomic gas has a different temperature from the dust mixed with the molecular gas. The color temperature inferred for the dust mixed with the atomic gas is $T_1 = 17.0 \pm 0.3 \text{ K}$, and for the dust mixed with the molecular gas it is $T_2 = 14.7 \pm 0.2 \text{ K}$.

3.4.3. Determination of the H_2 to CO Conversion Factor

The observation that atomic and molecular clouds have different infrared spectra implies that their relative column densities cannot be simply determined using observations at a single wavelength. This has an important practical implication. Naively, the ratio

$$X_{\text{naive}} = 0.5b/a \quad (7)$$

gives the column density of H_2 per unit CO line integral; values of X_{naive} are listed in the last column of Table 5. It is evident that the naively inferred value of X changes by a factor of 2 depending on the wavelength, which is inconsistent with the idea that the infrared emission is a linear tracer of the total column density. We can, however, calibrate this effect using the results obtained here. We assume that within the molecular phase, the gas is completely molecular and the dust-to-gas ratio is the same as in the atomic phase.

Then the column density of H_2 per unit CO line integral is

$$X = \frac{1}{2} \frac{b}{a} \frac{B_\nu(T_1)}{B_\nu(T_2)} \quad (8)$$

(Magnani & Onello 1995), which results in the last column of Table 5. When calibrated this way, a self-consistent

TABLE 5
MULTIPLE LINEAR REGRESSION BETWEEN INFRARED, H I, AND CO MAPS^a

WAVELENGTH (μm)	$a = I_\nu/N(\text{H I})$ ($\text{MJy sr}^{-1}/10^{20} \text{ cm}^{-2}$)	$b = I_\nu/W(\text{CO})$ ($\text{MJy sr}^{-1}/(\text{K km s}^{-1})$)	χ_ν^2	$X = N(\text{H}_2)/W(\text{CO})$ [$10^{20} \text{ cm}^{-2}/(\text{K km s}^{-1})$]	
				Naive	True
100	0.48 ± 0.02	0.34 ± 0.03	1.1	0.35 ± 0.05	1.3 ± 0.3
140	1.06 ± 0.08	1.24 ± 0.12	0.8	0.58 ± 0.11	1.5 ± 0.4
240	0.94 ± 0.06	1.33 ± 0.10	1.2	0.71 ± 0.11	1.3 ± 0.2

^a For the Ursa Major-Ursa Minor-Camelopardalis region.

description of the infrared emission from the atomic and molecular phases could be obtained from observations at a single wavelength—if the temperature contrast between the atomic and molecular components were the same everywhere. Clearly, observations at 240 μm are the best infrared tracer of molecular gas, because the 240 μm emission is less sensitive to temperature changes.

The H_2 column density per unit CO line integrated intensity has been measured by several techniques and for several different regions, with a fairly wide range of results. The “canonical” method is to correlate γ -ray emission—due to interaction of cosmic rays with nuclei—with the CO and H I emission simultaneously. This correlation has been performed in the galactic plane, where the CO emission is dominated by giant molecular clouds and $X = (2.3 \pm 0.3)$ has been found³ (Strong et al. 1988). The correlation of γ -ray emission and CO line brightness in the Ursa Major/Ursa Minor region yielded $X = (0.92 \pm 0.1)$ (Digel et al. 1996). The γ -ray method, like the “naive” infrared method, assumes that the γ -ray emission properties of the atomic and molecular clouds are the same. In fact, recent observations of lower energy γ -rays indicate that the value of X inferred depends on the energy of the γ -rays, with values ranging from 1.1 to 4 (Strong et al. 1994). If the difference is due to processes that only operate at low energies, then the “canonical” value of 2.3 holds, for it was determined at high energies; however, until this is understood, there remains the possibility that even the canonical X is uncertain by a factor of 2.

The infrared method of locating and estimating the column density of H_2 is especially useful because a wide range of physically different types of cloud can be observed. For the galactic center, Sodroski et al. (1995) found that the value of X is an order of magnitude lower than in the outer Galaxy. Their analysis takes into account the higher dust temperature in the galactic center, because they used the dust optical depth from 140 and 240 μm observations. At high latitudes, the molecular clouds are smaller, so one might anticipate a difference in the H_2 column density per unit CO line integrated intensity due to the higher radiation fields that can penetrate a smaller cloud.

An analysis very similar to our multiple linear regression was performed for the Ursa Major clouds using higher angular resolution 21 cm line observations with the Effelsberg 100 m telescope and IRAS 100 μm data (de Vries et al. 1987). Their infrared map clearly revealed the presence of the clouds that were not evident in the 21 cm line map, and the combined H I and CO maps were found to reproduce the infrared brightness, with $X_{\text{naive}} = (0.5 \pm 0.3)$. Using the temperature of atomic and molecular clouds we found for the entire north celestial pole region,

$$X = 3.8X_{\text{naive}} = (1.9 \pm 1.1) \times 10^{20} \text{ cm}^{-2} (\text{K km s}^{-1})^{-1}. \quad (9)$$

The corrected X for the Ursa Major clouds is consistent with the “canonically” adopted γ -ray results.

For some clouds, however, the H_2 column density per unit CO line integral is significantly different from canonical values. The cloud HRK 236+39 was observed in the 21 cm line with the Arecibo 305 m telescope, which provides the highest resolution single-dish observations of an isolated, diffuse interstellar cloud (Reach et al. 1994). For this cloud,

the linear regression of the H I, CO, and infrared maps resulted in the naively determined value $X_{\text{naive}} = (0.16 \pm 0.03)$. This low value is not due to a temperature effect: we find in the present work that the color temperature of the far-infrared excess emission is 16.5 K, only slightly colder than that of atomic gas. In order to explain the low X_{naive} with a temperature difference alone, the temperature of the molecular gas would have to be 13.2 K. While this might seem similar to the observed 16.5 K, it is in fact clearly ruled out: for the same 100 μm brightness, the 240 μm emission of the cloud would be more than 4 times brighter than observed. For HRK 236+39, comparison of the H I, CO, and infrared maps clearly shows that there is a component of the infrared emission that is not traced by H I 21 cm or CO (1 \rightarrow 0) line emission. The infrared excess exists in the central $\sim 45'$ of the cloud, while the CO is concentrated even more to the center, in clumps with size $\sim 2'$. Similar results have been found from a comparison of infrared and CO maps of the Chameleon region by Boulanger et al. (1998). They found that the large clouds, with extensive CO emission, $X_{\text{naive}} = (0.6\text{--}1.0)$, which could easily be explained by a somewhat lower dust temperature in the molecular clouds. The large scatter in the comparison of CO and extinction maps—which are independent of the dust temperature—was found to be due to spatially coherent regions where the gas is primarily H_2 but the CO abundance is low.

3.4.4. Comparison with Other Tracers of Molecular Gas

Any map of molecular gas, even over a very restricted region, would allow us to calibrate the infrared excess. Where it has been observed, the extinction of background starlight provides a temperature-independent tracer of the total column density. Comparison of extinction and CO maps for high-latitude clouds yields $X = (0.4\text{--}6.4)$ (Heithausen & Thaddeus 1990; Magnani, Blitz, & Wouterloot 1988), but it is unclear whether the large scatter is due to real cloud-to-cloud variations or calibration difficulties in the extinction maps (which are obviously uncertain when the extinction is appreciably more than unity). The H_2 molecule is symmetric, so that its rotational transitions must be quadrupolar, and the lowest energy transition has an energy of 500 K, which cannot be excited under typical interstellar conditions. Absorption-line studies are able to trace cold, diffuse gas, but the paucity of suitable background stars makes comparison with large-beam observations problematic. A promising method is to observe the low-energy radio transitions of the CH molecule, because CH forms readily—but only where the H is molecular. Magnani & Onello (1995) have observed a set of both translucent and dark molecular clouds in the 9 cm lines of CH and used the empirical correlation of CH line brightness with extinction to obtain the H_2 column density. They find that $X = (0.3\text{--}6.8)$ for translucent high-latitude clouds, a substantial range, as was found from the extinction studies. The value of X was also found to vary within clouds, where it was observed for more than one position. A detailed comparison of our results with those of Magnani & Onello (1995) is complicated because the clouds are structured on scales smaller than our beam, while the CH lines have not been mapped over the clouds. While there is clearly an infrared excess counterpart of each of the clouds in their sample, only 11 lines of sight are suitable for comparison; we find that the ratio of 240 μm infrared excess to H_2

³ Units for X throughout this paper are $10^{20} \text{ cm}^{-2} (\text{K km s}^{-1})^{-1}$.

column density (inferred from the CH line brightness) ranges from 0.4 to 2 MJy sr⁻¹/(10²⁰ cm⁻²). It is unclear whether the range of values is due to beam size effects or a true variation from cloud to cloud, but this comparison at least affords a calibration of the infrared excess independent of CO. For comparison, the calibration of 240 μm emission per H₂ for the north celestial pole region yields

$$I_{\nu}(240 \mu\text{m})/N(\text{H}_2) = b/X = 1.0 \pm 0.2 \text{ MJy sr}^{-1} \\ \times (10^{20} \text{ cm}^{-2})^{-1} \quad (10)$$

using Table 5, which is within the range given by the CH calibration.

Future molecular observations of our sample clouds will allow another step toward understanding their nature. Presuming that the infrared excess really does indicate the presence of H₂, measuring the column densities of other species will reveal their chemistry. In particular, CO is a very robust molecule that, once formed, becomes the dominant gas-phase molecular form of O and C. Other molecules that we expect to form in abundance include OH and CH. As mentioned above, CH forms early and is thought to be a linear tracer of H₂. The chemistry of these molecules is dictated by photodissociation, so one may define a critical column density above which a molecule is produced more rapidly than it is destroyed. Diffuse and translucent clouds such as the infrared excess clouds found in this paper are likely to have column densities not much larger than the critical column density for CO. Blitz, Bazell, & Désert (1990) have surveyed CO (1 → 0) emission toward one or two positions in about half of the infrared excess clouds from the DBB study. They found a surprisingly low detection rate (13%) of CO emission and saw evidence for a threshold such that CO emission is present only in clouds with more than 4 MJy sr⁻¹ of 100 μm emission. Using our calibration of infrared excess emission, we find that the Blitz et al. threshold corresponds to a visual extinction of about 1.6 mag. The lower column density clouds could be members of a CO-poor class of diffuse clouds (Lada & Blitz 1988) in which the CO cannot self-shield. These tentative conclusions need to be confirmed with future observations, because we have found significant differences between our infrared excess catalog and that of DBB, and because one or two positions per cloud with a small beam may not suffice to detect highly structured CO emission. Detailed studies of individual clouds may better reveal the physical processes: the onset of CO self-shielding should be evident in radial profiles or confinement of CO emission to the centers of clouds (Reach et al. 1994), and the effect of central condensation on the CO excitation can be estimated using three-dimensional models of clouds (Spaans & Neufeld 1997).

4. CONCLUSIONS

The infrared excess clouds, which were found after removing emission associated with the atomic interstellar medium, are predominantly molecular clouds. The dust in these clouds is colder than dust in diffuse atomic clouds, for

the same reason that the gas is molecular: the outer layers of the cloud shield the center from the dust-heating and molecule-dissociating effects of the interstellar radiation field. These molecular clouds fill only a small fraction of the high-latitude sky.

The column density of the infrared excess clouds can be estimated using the calibrations discussed above, which may be rewritten as

$$I_{100}^{\text{ex}}/N(\text{H}_2) = 0.26 \pm 0.05 \text{ MJy sr}^{-1}(10^{20} \text{ cm}^{-2})^{-1}. \quad (11)$$

We can estimate the mass surface density of the infrared excess clouds, using the difference between positive and negative excess for $|b| > 20^\circ$ (Fig. 6). The surface density is about 0.3 $M_\odot \text{ pc}^{-2}$ (including 40% He by mass), roughly equally partitioned among regions of low and high brightness. (We adjusted for the part of the sky at $|b| < 20^\circ$ by assuming it has the same average infrared excess as the rest of the sky.) The mass density that we find is an order of magnitude larger than that found in an unbiased, wide-field CO survey (Hartmann et al. 1998) of the northern sky, but it is comparable to a previous estimate—also based on CO—of the total mass of the known molecular clouds at high galactic latitude (Magnani et al. 1996). A CO survey would miss molecular gas that is deficient in CO or regions where the CO rotational levels are subthermally excited (because of low H₂ volume density). We do *not* find a great disparity between the northern and southern galactic hemispheres (cf. Hartmann et al. 1998); according to the infrared excess, the southern galactic hemisphere has about 30% more molecular gas than the northern hemisphere. The high-latitude infrared-excess clouds make up a significant fraction of the total mass of molecular gas in the solar neighborhood.

The infrared excess maps can be used to provide a guide to regions of anomalously high extinction. The extinction calculated from the H I column density (cf. Burstein & Heiles 1978) can significantly underestimate the total extinction in these regions. If we assume that the dust in the infrared-excess clouds has the same extinction cross section per H-nucleus as diffuse clouds for which this quantity has been measured (Bohlin, Savage, & Drake 1978), then the extinction due to infrared excess clouds can be obtained from Figure 7, after multiplying the 100 μm surface brightness by $A_V/I_{100}^{\text{ex}} \sim 0.027 \text{ mag MJy}^{-1} \text{ sr}$.

WTR was supported by NASA's COBE project during the early part of this work, through a contract to the Universities Space Research Association. In searching for counterparts for the objects found in this work, we use the SkyView facility at NASA Goddard Space Flight Center; SkyView is supported by NASA ADP grant NAS 5-32068. We also made use of the SIMBAD database, which is maintained by the Centre de Données astronomiques de Strasbourg (CDS), France. We thank Xavier Désert, François Boulanger, Rick Arendt, Janet Weiland, Tom Sodroski, and Mike Hauser for their comments and suggestions.

REFERENCES

- Arendt, R. G., et al. 1998, ApJ, submitted
 Blitz, L., Bazell, D., & Désert, F. X. 1990, ApJ, 352, L13
 Blitz, L., Magnani, L., & Mundy, L. 1984, ApJ, 282, L9
 Boggess, N. W., et al. 1992, ApJ, 397, 420
 Bohlin, R. C., Savage, B. D., & Drake, J. F. 1978, ApJ, 224, 132
 Boulanger, F., Abergel, A., Bernard, J., -P., Burton, W. B., Désert, F.-X., Hartmann, D., Lagache, G., & Puget, J.-L. 1996, A&A, 312, 256
 Boulanger, F., Bronfman, L., Dame, T. M., & Thaddeus, P. 1998, A&A, 332, 273
 Boulanger, F., & Pérault, M. 1988, ApJ, 330, 964
 Burstein, D., & Heiles, C. 1978, ApJ, 225, 40
 Cleary, M. N., Heiles, C., & Haslam, C. G. T. 1979, A&AS, 36, 95
 Désert, F. X., Bazell, D., & Boulanger, F. 1988, ApJ, 334, 815
 Désert, F. X., Boulanger, F., & Puget, J.-L. 1990, A&A, 327, 215

- de Vries, H. W., Thaddeus, P., & Heithausen, A. 1987, *ApJ*, 319, 723
- Digel, S. W., Grenier, I. A., Heithausen, A., Hunter, S. D., & Thaddeus, P. 1996, *ApJ*, 463, 609
- Draine, B. T., & Lee, H. M. 1985, *ApJ*, 285, 89
- Dwek, E., et al. 1998, *ApJ*, in press
- ESA 1997, *The Hipparcos and Tycho Catalogues*, ESA SP-1200
- Gir, B.-Y., Blitz, L., & Magnani, L. 1994, *ApJ*, 434, 162
- Hartley, M., Tritton, S. B., Manchester, R. N., Smith, R. M., & Goss, W. M. 1986, *A&AS*, 63, 27
- Hartmann, D., & Burton, W. B. 1997, *Atlas of Galactic Neutral Hydrogen* (Cambridge: Cambridge Univ. Press)
- Hartmann, D., Kalberla, P. M. W., Burton, W. B., & Mebold, U. 1996, *A&AS*, 312, 256
- Hartmann, D., Magnani, L., & Thaddeus, P. 1998, *ApJ*, 492, 205
- Hauser, M. G., Kelsall, T., Leisawitz, D., & Weiland, J. L., ed., *COBE Diffuse Infrared Background Experiment Explanatory Supplement, version 2.1*, *COBE* reference publication 97-A (Greenbelt: NASA/GSFC) (available in electronic form from the National Space Science Data Center)
- Hauser, M. G., et al. 1998, *ApJ*, in press
- Heiles, C., & Habing, H. J. 1974, *A&AS*, 14, 1
- Heiles, C., Reach, W. T., & Koo, B.-C. 1988, *ApJ*, 332, 313 (HRK)
- Heithausen, A., Stacy, J. G., de Vries, H. W., Mebold, U., & Thaddeus, P. 1993, *A&A*, 268, 265
- Heithausen, A., & Thaddeus, P. 1990, *ApJ*, 353, L49
- Israel, F. P., Bontekoe, T. R., & Kester, D. J. M. 1996, *A&A*, 308, 723
- Kawara, K., et al. 1997, in *Diffuse Infrared Radiation and the IRTS*, ed. H. Okuda, T. Matsumoto, & T. Rollig (San Francisco: ASP), 386
- Kelsall, T., et al. 1998, *ApJ*, submitted
- Keto, E. R., & Myers, P. C. 1986, *ApJ*, 304, 466
- Kulkarni, S. R., & Heiles, C. 1988, in *Galactic and Extragalactic Radio Astronomy*, ed. G. L. Verschuur & K. I. Kellermann (2d ed.; Berlin: Springer), 95
- Lada, E. A., & Blitz, L. 1988, *ApJ*, 326, L39
- Lagache, G., Abergel, A., Boulanger, F., & Puget, J.-L. 1998, *A&A*, 333, 709
- Laureijs, R. J., Haikala, L., Burgdorf, M., Clark, F. O., Liljeström, T., Mattila, K., & Prusti, T. 1996, *A&A*, 315, L317
- Low, F. J., et al. 1984, *ApJ*, 278, L19
- Magnani, L., Blitz, L., & Mundy, L. 1985, *ApJ*, 295, 402 (MBM)
- Magnani, L., Blitz, L., & Wouterloot, J. G. A. 1988, *ApJ*, 295, 402
- Magnani, L., Hartmann, D., & Speck, B. G. 1996, *ApJS*, 106, 447
- Magnani, L., Lada, E. A., & Blitz, L. 1986, *ApJ*, 301, 395
- Magnani, L., & Onello, J. S. 1995, *ApJ*, 443, 169
- McCammon, D., & Sanders, W. T. 1990, *ARA&A*, 28, 657
- Mochizuki, K., Nakagawa, T., Doi, Y., Yui, Y., Okuda, H., Shibai, H., Yui, M., Nishimura, T., & Low, F. 1994, *ApJ*, 430, L37
- Moshir, M., et al. 1992, *Explanatory Supplement to the IRAS Faint Source Survey, version 2* (Pasadena: JPL)
- Neugebauer, G., et al. 1984, *ApJ*, 278, L1
- Odenwald, S., Newmark, J., & Smoot, G. 1997, preprint astro-ph/9610238
- Puget, J.-L., Abergel, A., Bernard, J.-P., Boulanger, F., Burton, W. B., Désert, F.-X., Hartmann 1996, *A&A*, 308, 5
- Puget, J.-L., et al. 1998, *A&A*, submitted
- Reach, W. T., Franz, B. A., Kelsall, T., & Weiland, J. L. 1996, in *Unveiling the Cosmic Infrared Background*, ed. E. Dwek (New York: AIP), 37
- Reach, W. T., Heiles, C., & Koo, B.-C. 1993, *ApJ*, 412, 127
- Reach, W. T., Koo, B.-C., & Heiles, C. 1994, *ApJ*, 429, 672
- Reach, W. T., Wall, W. F., Hauser, M. G., Sodroski, T. J., Odegard, N., & Weiland, J. L. 1994, *BAAS*, 185, 57.09
- Reynolds, R. J. 1985, *AJ*, 90, 92
- Savage, B. D., Bohlin, R. C., Drake, J. F., & Budich, W. 1977, *ApJ*, 216, 291
- Schlegel, D., Finkbeiner, D. P., & Davis, M. 1998, *ApJ*, 500, 525
- Shafer, R., et al. 1998, in preparation
- Snowden, S. L., McCammon, D., & Verter, F. 1995, *ApJ*, 309, L21
- Sodroski, T. J., et al. 1995, *ApJ*, 452, 262
- Spaans, M., & Neufeld, D. A. 1997, *ApJ*, 484, 785
- Strong, A. W., et al. 1994, *A&A*, 292, 82
- . 1988, *A&A*, 207, 1
- van Buren, D., & McCray, R. 1988, *ApJ*, 336, L67
- Wakker, B. P., & Boulanger, F. 1986, *A&A*, 170, 84
- Wall, W. F., et al. 1996, *ApJ*, 456, 566
- Wang, Q. D., & Yu, K. C. 1995, *AJ*, 109, 698
- Zagury, F. 1997, Ph.D. thesis, Université Paris-Sud (Orsay, France)